2015

Highly scalable bio-inspired soft elastomeric capacitor for structural health monitoring applications

Hussam Suhail Saleem
Iowa State University

Highly scalable bio-inspired soft elastomeric capacitor for structural health monitoring applications

by

Hussam Saleem

A dissertation submitted to the graduate faculty

in partial fulfillment of the requirements for the degree of

DOCTOR OF PHILOSOPHY

Major: Civil Engineering (Structural Engineering)

Program of Study Committee:
Simon Laflamme, Major Professor
Aleksandar Dogandzic
Jeremy Ashlock
Terry Wipf
Tian Jin
Filippo Ubertini

Iowa State University

Ames, Iowa

2015

DEDICATION

To my late father, who dedicated his life for his family.

To my loving mother for her support all these years.

To my brothers, sisters, brothers in law and sisters in law.

TABLE OF CONTENTS

LIST OF FIGURES

LIST OF TABLES

ACKNOWLEDGEMENTS

The completion of my PhD would not have been possible without the help and guidance of my advisor, professors, and fellow graduate students with whom I have worked with over the past three years.

I would like to express my thanks and appreciation to my advisor Dr. Simon Laflamme for giving me the opportunity, support, guidance, and motivation to conduct this study and accomplish my goals. Also, I want to thank my committee members for their help in guiding me through this trip.

A special thanks goes to Dr. Mahendra Thunga and Dr. Matthias Kolloche, who provided me with all the training required for this study; in both theoretical and experimental aspects, they helped me every step on the way.

I would also like to recognize the support of my family and friends throughout the challenging, but rewarding process of this achievement.

Lastly, The development of the SEC technology is supported by grant No. 1001062565 from the Iowa Alliance for Wind Innovation and Novel Development and grant No. 13-02 from the Iowa Energy Center. Their support is gratefully acknowledged.

ABSTRACT

Over the past few decades, Structural Health Monitoring (SHM) has gained wide popularity as it became essential to integrate monitoring systems into complex structural systems to ensure structural integrity and minimize hazards that may arise from any structural failure or collapse. Current monitoring technologies are capable of monitoring small areas with a priori information about the location of an existing defect, therefore they lack the ability to efficiently monitor large scale systems such as bridges and wind turbine blades. The objective is to create a system capable of performing real-time online SHM with continuous feedback. This research aims at developing a complete system for structural health monitoring of wind turbine blades, including the sensing element, the data acquisition system, and the damage detection algorithm. The proposal is a network of soft sensors covering large surfaces capable of monitoring global as well as local behavior. The advantages of such a solution include cost efficiency, customizability in size and shape to accommodate the application, simple fabrication and installment and direct feature extraction with simple signal processing and machine learning techniques. The studies conducted to complete this dissertation intended to develop the sensing element (material and fabrication), characterize it and demonstrate applications to real structures. The proposed sensing element is a novel soft elastomeric capacitor (SEC) sensor for monitoring of large surfaces, applicable to composite materials. This soft capacitor is fabricated using a highly sensitive elastomer sandwiched between electrodes. It transduces strain into changes in capacitance. The elastomer is made of a Styrene Ethylene Butylene Styrene (SEBS) polymer doped with high permittivity Titanium dioxide (TiO_2) as a filler material to increase the overall composite permittivity and

improve the durability. The electrodes are made of a similar polymer doped with carbon-black particles. The first study was conducted on optimizing the fabrication process for the sensor. We investigated the influence of processing methods that dictate the performance enhancement in a nanocomposite soft capacitor. The efficiency of ultrasonic probe and high-shear melt mixing methods in dispersing TiO_2 nanoparticles in SEBS polymer matrix was studied. The compression-molding method shows highly promising for engineering applications by enhancing fabrication speed, safety, and improving control over the film thickness.

The second part investigated the influence of interfacial treatment on the matrix-filler interaction using a melt-mixing process to fabricate robust and highly stretchable elastomers. Silicone oil and silane coupling agent were studied as possible solutions to enhance the compatibility between the inorganic fillers and polymer matrix. Results showed that specimens filled with silicone oil coated particles have promising overall properties. The third part, consisted of several experiments to characterize the functionality and applicability of the SEC to implement SHM to real life structures. The sensor behavior under static and dynamic loads was evaluated. Static test results showed the capability of the sensor to measure strains above 25 $\mu\varepsilon$ with an almost linear behavior up to 20% strain levels and a gauge factor of 2. Dynamic results showed capability to accurately detect frequency contents and mode shapes. All the characterization tests were verified with one or more method, including commercial strain gauges, accelerometers and finite element models. Using SECs in a network configuration have a great potential to implement an efficient inexpensive real time SHM on large-scale structures such as wind turbine blades. SEC data can be used to perform damage detection, localization and prognosis based on statistical as well as vibration analysis.

CHAPTER 1. INTRODUCTION

1.1 Background

Structural systems including bridges, buildings, aerospace structures and wind turbines are susceptible to age, deterioration and damage. Structural damage identification implemented through Structural health monitoring (SHM) has gained attention recently due to its importance in ensuring integrity and safety of structural systems and prevent unpredictable structural failures that may cause human and economical losses. SHM is defined as the process of implementing a damage identification strategy for aerospace, civil and mechanical engineering infrastructure [Farrar and Worden, 2007]. It aims at diagnosing, localizing, and prognosing structural damages. In this process damage is measured as a change from an initial state which is referred to as the healthy state to a new state with a different structural behavior, changes might be in material properties, geometry or both. These changes result in a corresponding variation in a specific structural property such as stiffness, fundamental frequency and damping. Current maintenance techniques are often implemented on a timely basis and are conducted by visual inspection and nondestructive evaluation (NDE) techniques, such as X-rays, optical coherence tomography, Eddy current, and laser strain [B. Srensen and Rusborg, 2002, Jones, 2009]. The time based maintenance must evolve to a condition based maintenance [Farrar and Worden, 2007]. To accomplish this and to overcome these technological limitations, an online real time system that can perform continuous monitoring is required [Worden and Dulieu-Barton, 2004]. Solution have been proposed using real-time sensors such as

accelerometers, strain gauges and fiber optics. [Lading et al., 2002, Chang et al., 2003]

several technologies were studied and implemented in the area of structural health monitoring in the pursuit of a reliable system capable of implementing all the levels of damage identification . These can divided into four levels, as follows [Rytter, 1993]:

Level 1: Determination of the existence of damage;

Level 2: Determination of the geometric location of the damage;

Level 3: Quantification of the severity of the damage;

Level 4: Prediction of the remaining service life of the structure.

Levels 1-3 can be described as the damage diagnosis stage while level 4 is the prognosis stage. As we move from level 1 to 4, the degree of complexity increases and a need for a mathematical or a damage model is necessary to predict damage. [C.R. Farrar and Robertson, 2003].

Researchers developing health monitoring systems have utilized different types of sensors as sensing elements to overcome the limitations faced when using other techniques like NDE; these include fiber optic sensors and piezoelectric sensors to measure quantities such as strain, acceleration and displacement. Fiber optic sensors excel in providing reliable dense measurements with high accuracy, and low noise contents [Michie et al., 1997]. In addition it can be easily embedded in civil structures to flexible shapes. piezoelectric sensors such as the lead zirconate titanate (PZT) can be used to measure several quantities including vibration, strain and waves. They are very sensitive to damage and have low sensitivity to noise (high signal to noise ratio). Other researchers have proposed utilizing a single or a combination of the aforementioned sensing technologies. [Maenaka, 2008] proposed using MEMS inertial sensors,these sensors included an accelerometer and a gyroscope. Advantages of these sensors are the small size, low cost, three dimensional sensing and ability to be mass produced. [Baptista et al., 2009] used an impedance measurement system for lead zicronate titnate (PZT) for their linearity, resistance to temper-

ature changes, low power consumption and low cost. [Thomson et al., 2009] proposed the use of passive wireless based sensor based on radio-frequency cavities. [Arms et al., 2009] proposed the use of an integrated system that includes strain gauges, accelerometeers, thermocouples, gyroscopes, accelerometers, magnetometers and GPS to get precise measurements. [Zhang et al., 2010] used Micro-Opto-Electro-Mechanical systems (MOEMS) acoustic sensors to detect acoustic emissions for SHM applications. Others have proposed using surface skin-type sensors [Gao et al., 2010,Kang et al., 2006,Srivastava et al., 2011]. Examples are resistive and capasitive based sensors. Capacitive-based technologies include applications to humidity, pressure, strain, and tri-axial measurements [Hong et al., 2012, Lipomi et al., 2011, Arshak et al., 2000, Suster et al., 2006, Dobrzynska and Gijs, 2013].

Strain is one of the simplest measurements that is conducted on any structure. Defined as the change in length per unit length, changes in strain can be directly related to changes in the material properties, therefore is a good candidate for health monitoring. Measuring total strain is not a representative indication of reaching a failure point in a structure though, therefore a network of strain measuring devices need to be installed to get a dense map of strain readings in local areas. And even this may be insufficient [Balageas et al., 2006].

Strain sensors can be divided into two types of sensors; electrical and fiber optic. The electrical sensors have become to be the most dominant and widely accepted type in the strain measurement area [Schubel et al., 2013]. with the electrical resistance to be the most popular for most types of structures and is considered the most mature [Balageas et al., 2006]. Other electrical sensors include capacitance, inductance, and semiconductor-based sensors. Each type is related to a specific electrical property change [Balageas et al., 2006]. Fiber optic sensors can be classified into three three types based on their technique of utilization. Those include; Intensity based fiber optic, phase modulated optical fiber sensors, or interferometers, and wavelength based sensors, or Fiber Bragg

Gratings (FBG). A more comprehensive review can be found in [Schubel et al., 2013].

There is numerous research on using strain sensors for SHM applications, for instance [Choi et al., 2008] used strain gauges in a wireless network. strain gauges are attractive due to their low cost, ease of use and installation, and high sensitivity. [Michie et al., 1997] proposed using fiber optic sensors to evaluate structural integrity.

1.2 Problem Statement

SHM of mesosystems mentioned before, is particularly a challenging task due to the large geometrical size and complexity of the monitored systems [Laflamme et al., 2014]. Most of the systems available cannot handle such size and complexity. To overcome the technological limitation, a new system 1) capable of monitoring large surfaces, 2) perform real time measurements and 3) cost effective is essential.

1.3 Contribution and Objectives

The proposed solution is a novel sensing technology specifically designed to be highly scalable. It consists of a network of soft elastomeric capacitors (SEC), fabricated from an inexpensive nanocomposite customizable in shapes and sizes [Laflamme et al., 2013a, Laflamme et al., 2012]. Each SEC consists of a dielectric layer made of a polymer and a filler to enhance its properties and covered with two conductive layers forming the electrodes. The sensing principle is based on the fact that a change in geometry in the SEC tranduces into a measurable change in its capacitance. Arranged in a network configuration, the sensing technology can measure discrete deformations over a large area, analogous to biological skin, providing local as well as global feature extraction capabilities.

This research have three main objectives.

1) Develop a fabrication process for the SEC.

2) Investigate and optimize the material composition of the SEC.

3) Characterize the behavior of the sensor and its applications statically and dynamically.

1.4 Electro-Mechanical Model

The SEC is designed to be adhered onto the monitored surface along its $x-y$ plane (Fig. 1.1b). Assuming low frequency measurements (< 1 kHz), the transducer can be considered as a non-lossy capacitor with capacitance C

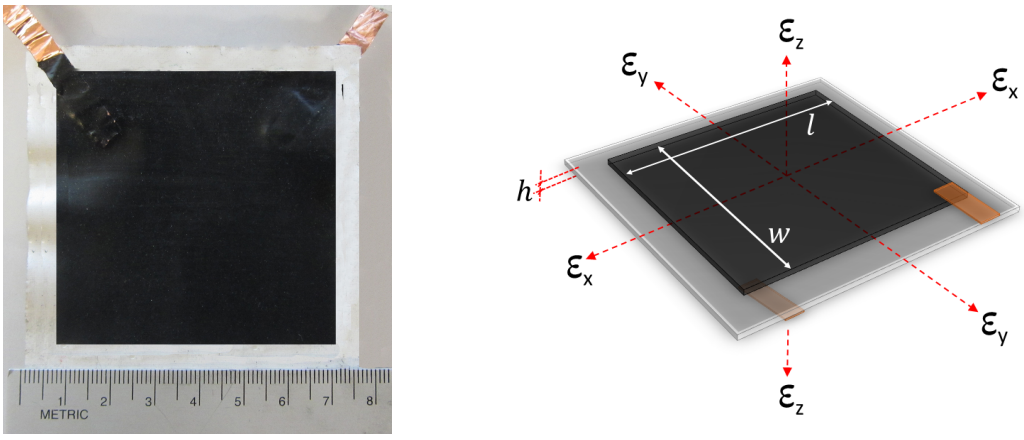

(a) (b)

Figure 1.1: A soft elastomeric capacitor (SEC)

$$C = e_0 e_r \frac{A}{h} \tag{1.1}$$

where $e_0 = 8.854$ pF/m is the vacuum permittivity, e_r is the polymer relative permittivity, A is the area of the sensor area of width w and length l, and h is the thickness of the dielectric. Assuming small strain, one can take the differential of Eq. (1.1)

$$\frac{\Delta C}{C} = \left(\frac{\Delta l}{l} + \frac{\Delta w}{w} - \frac{\Delta h}{h}\right) = \varepsilon_x + \varepsilon_y - \varepsilon_z \tag{1.2}$$

where ε_x, ε_y and ε_z are strains in the x, y and z directions as shown in Fig. 1.1b(b). An expression relating ε_z to ε_x and ε_y can be obtained using Hooke's law for in-plane stress

$$\varepsilon_z = -\frac{\nu}{1-\nu}(\varepsilon_x + \varepsilon_y) \tag{1.3}$$

The final form of the electromechanical model is obtained by integrating Eq. 1.3 in Eq. 1.2

$$\frac{\Delta C}{C} = \lambda(\varepsilon_x + \varepsilon_y) \tag{1.4}$$

where $\lambda = \frac{1}{1-\nu}$ represents the gauge factor of the sensor. For SEBS, $\nu \approx 0.49$ [Wilkinson et al., 2004], which gives a gauge factor $\lambda \approx 2$.

1.5 Thesis Organization

The thesis is organized as follows. Chapter 2 describes two proposed fabrication processes and discusses the advantages and disadvantages of both. Chapter 3 describes the investigation conducted to to find an optimized material composition for enhanced thermal, morphological, mechanical and electrical properties for the SEC and presents the findings. Chapter 4 presents the static and dynamic characterization conducted for the SEC. Chapter 5 presents the conclusions and future work.

CHAPTER 2. FABRICATION PROCESS

This chapter has been disseminated at the QNDE conference in the publication **"BIO-INSPIRED SENSORY MEMBRANE: FABRICATION PROCESSES FOR FULL-SCALE IMPLEMENTATION"**

2.1 Introduction

Elastic polymer materials are an attractive choice due to their mechanical properties and convenient processing techniques. Soft dielectric membrane has to fulfill engineering and measurement requirements to allow an easy installation and electronic evaluation. This requirement can be fulfilled with tailored nanocomposites. A polymer composite is to embed high dielectric ceramic fillers in the soft polymer matrix to enhance its dielectric response and stiffness. The authors have studied the effect of adding nanoparticles to soft dielectric actuators and evaluated the possibility of improving the performance in terms of electrical as well as mechanical properties [Stoyanov et al., 2011].

Block copolymers (BCP) are suitable materials to use as a soft polymer matrix to prepare nanocomposites due to its heterogeneous phase separation at nanometer scales [Ren et al., 2000, Krishnamoorti et al., 2001, Laurer et al., 1996, Silva et al., 2001, Lee et al., 2003, Mani et al., 2000, Mischenko et al., 1994, Hashimoto et al., 1981, Van Dijk and Van den Berg, 1995] . BCP's have shown more control on the spatial and orientational distribution of the nanoparticles [Bockstaller et al., 2005]. The dispersion of the ceramic fillers contributes to enhancing the physical and mechanical properties of the sensors.

It follows that the interaction between the polymer matrix and the filler becomes very critical when dealing with nanoparticles.

Here, to improve robustness and further reduce costs associated with our sensing method, we studied the fabrication process of the nanocomposite. We used a styrene-based Poly(styrene-ethylene/butylene-styrene) (SEBS) BCP filled with Titanium dioxide (TiO_2) nanoparticles. SEBS is a soluble tri-block copolymer considered under the class of thermoplastic elastomers in polymeric materials.

Despite unique advantages of using the TiO_2 fillers in SEBS, the non-polar nature of SEBS BCP severely limits the dispersion of polar TiO_2 particles in the polymer matrix. To overcome the problem with dispersion, Ganguly *et al.* have suggested modifying the SEBS by grafting polar functional groups in their case maleic anhydride. This chemical modification resulted in enhancing the surface interaction between the polymer matrix and filler particles resulting in improving the material properties (Polymeric Nanocomposites of Polyurethane Block). Similarly, the surface chemistry of the fillers was changed to attain fine dispersion of the fillers in the matrix [Ganguly et al., 2006][18] . In addition to the passivation of either filler or polymer matrix for getting fine dispersion, the processing methods play a key role in dispersing the nanoparticles.

In this chapter, we evaluated polymer processing techniques including Melt-Mixing fabrication and a direct liquid cast on the mechanical and dielectric properties of the soft dielectric. The melt-mixing is favorable since it avoids the use of any kind of organic solvents or dispersing technique such as sonication. Instead a micro compounder is utilized to mix the polymer with the nanoparticles under a specified temperature. The results from the latter method are compared with those from the drop-cast method and discussed in details.

2.2 Experimental

2.2.1 Materials

The thermoplastic matrix material SEBS-Mediprene 500120 M, (poly-Styrene-co-Ethylene-co-Butylene-co-Styrene) was purchased from VTC Elastoteknik AB, Sweden. (density = 930 kg/m). Rutile titania (TiO_2) namely R320, R320D (Sachtleben Chemie GmbH (Germany), were used as high permittivity fillers. The TiO_2 particles have an average diameter of 300 nm and density = 4200 kg/m3. While R320 is uncoated, R320D is coated with silicone oil (PDMS). Bis[3-(triethoxysilyl)propyl]tetra sulfide, a silane coupling agent commonly used as a rubber additive, was purchased from Santa Cruz Biotechnology, Inc. Dallas, Texas, U.S.A. Figure.3.6 shows a scanning electron microscopy (SEM) image of R320 powder (a) and its crystal structure (b), showing a distribution of spherical and ellipsoidal shaped particles. Such particles exhibit a highly anisotropic static dielectric [Stoyanov et al., 2011]. Figure. 2.1b is a schematic of R320, showing that a high permittivity resulting from the crystalline structure of TiO_2. Such structure generates polarization in the material, which increases the dielectric constant.

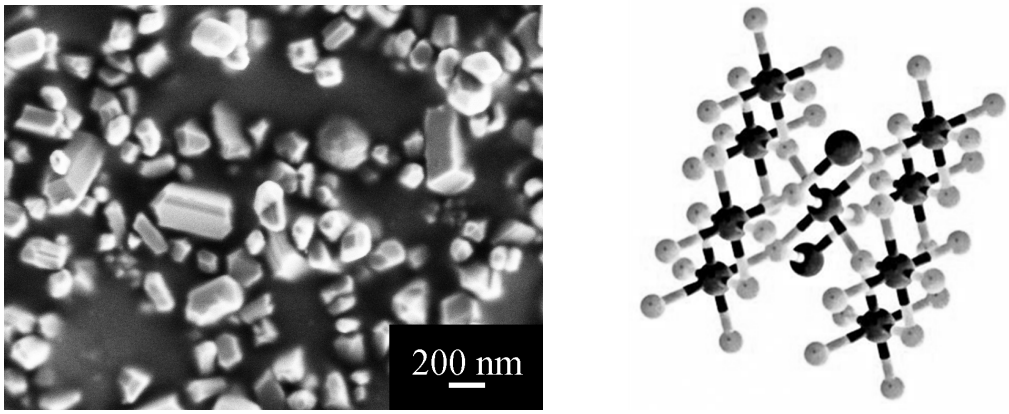

(a) (b)

Figure 2.1: a) Field effect SEM image of rutile TiO_2 powder R 320 b) Crystal structure of TiO_2, titanium and oxygen are represented by the larger and smaller balls respectively.

2.2.2 Fabrication processes

In order to study the influence of fabrication processes on the properties of the sensors, the samples were prepared by solution casting and melt processing [1]. Using the solution casting process, the fabrication process of the SEC is as follows. First, polystyrene-ethylene-butadiene-styrene (SEBS, Mediprene Dryflex) is dissolved into toluene. Second, the resulting solution is mixed with 15 vol% of titanium dioxide (titania or TiO_2, Sachtleben R 320 D) nanoparticles to increase the materials' robustness and permittivity. Third, the particles are uniformly dispersed within the polymer matrix using a sonic dismembrator (Fisher Scientific Model 120 Sonic Dismembrator) for 10 minutes. Fourth, the resulting solution is cast onto a 80 $\times$ 80 mm^2 flat glass plate to create the dielectric. Fifth, during the drying of the dielectric mix, another SEBS solution is mixed with a 10 vol% concentration of carbon black (CB) particles, and sonicated in a sonication bath for 6 hours. Finally, the conductive mix is painted on the top and bottom surfaces of the dried dielectric to create the compliant electrodes. During the drying process of the electrodes, copper tape is embedded in the SEBS+CB mix to create the physical connection to the DAQ. Fig. 1.1a is a picture of the resulting SEC.

[1] A more detailed fabrication process explanation is available in appendix A.

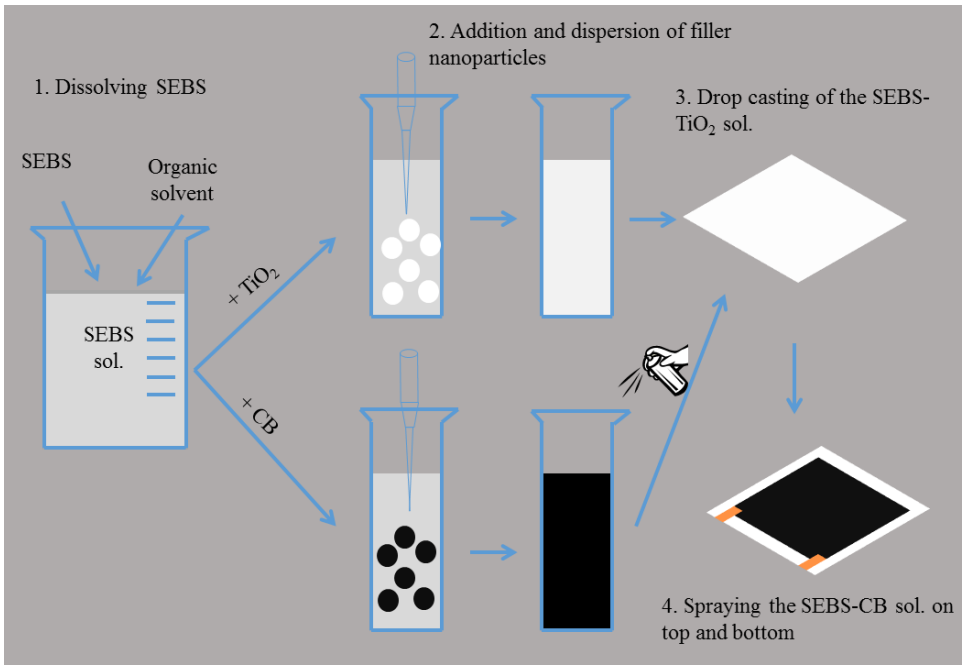

Figure 2.2: Solution casting fabrication process

All the investigated nanocomposite samples processed by melt mixing are prepared at 160^{o}C in a 30 ml capacity ATR (Advanced Torque Rheometer) Plasti-Corder heated shear mixer from C.W. Brabender Instruments, Inc., NJ. Figure. 2.3 illustrates the procedure used to prepare the test specimens using melt mixing method. TiO_2 was blended with SEBS under constant speed of the twin mixing screws at 50 rpm. The residence time of the melt in the barrel was limited to 10 min to avoid thermal degradation of the melt. The extruded SEBS-TiO_2 melt was processed into 200 m thick films by compression molding at 160 ^{o}C for 5 min. The sample was left at room temperature to anneal before releasing the pressed plates. Similarly, samples with Si-69 were fabricated by adding and dispersing the coupling agent in the SEBS prior to the adding the TiO_2. An average thickness of the pressed films was measured using a micrometer screw.

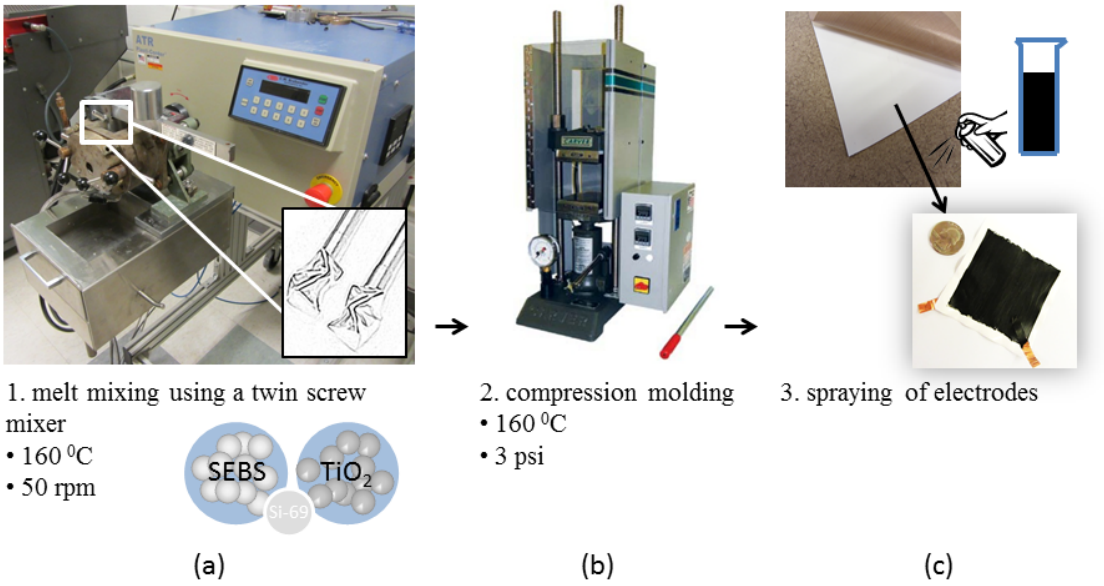

Figure 2.3: Melt mixing fabrication method: a) melt mixing, b) thermal compression molding, and c) final pressed film

2.2.3 Characterization

The morphology of the SEBS and SEBS nanoparticles was investigated by scanning electron microscopy SEM using a Hitachi S-2460N variable pressure SEM (VP-SEM) under helium atmosphere. The SEM images were collected at an accelerating voltage of 4, 8 and 20kV and from a working distance of 25 mm. The SEM images were collected from the cryo-fractured surfaces prepared in liquid nitrogen (LN2). The relative permittivity was measured for the films after adding layers of electrodes on the top and bottom of the films. The electrodes were 15% volume percentage carbon black (printex XE 2-B) in SEBS-Dryflex 500040. An LCR meter was used to measure the capacitance at 40Hz frequency and then back calculate the permittivity of the elastomer. Thermogravimetric analysis (TGA) on the nanocomposites was conducted with a TA Instruments Q50 thermogravimetric analyzer (New Castle, DE). The TGA samples were heated from 30 ^{o}C to 600 ^{o}C to study the residual wt.% after complete degradation of the nanocomposites.

Tensile tests were performed using an Instron universal testing machine (model 5569) with a ±2 kN load cell at room temperature (23 ± 2 °C) with a test speed of 5 mm/min. The tests were conducted on dog-bone sample with a gauge length of 30 mm. The samples for tensile tests were prepared by stamping dog-bone shape specimens according to ISO 527 type 5A.

2.3 Results and Discussion

2.3.1 Morphology

The post-fracture surfaces of the investigated sensor films processed by solution cast and melt-mixing techniques are shown in Figure. 2.4. The micrographs were taken from the center of the specimen. The high magnification images covering the overall fracture surface on the specimen are also shown to the right of the corresponding micrograph. The TiO_2 particles blended in the investigated samples are expected to have a slightly ellipsoidal shape as revealed previously from SEM investigations [Hadži, 1961]. The rutile titanate ceramic particles have a slightly ellipsoidal shape and the static dielectric properties are found to be highly anisotropic, with static dielectric properties of 86 along the axes a and b and 170 along c [Stoyanov et al., 2011].

The high magnification images in Figure. 2.4 represents the nature of nanoparticle dispersion in solution-casted and melt mixed sample respectively. As a result of fracturing the samples under cryogenic conditions, the overall fracture surface in both the micrographs appear to be brittle in nature. From the high magnification images, a significant difference in the nature of dispersion of the nanoparticles can be noticed in both the samples. The dispersion of nanoparticles in SEBS-MM-TiO_2 is free from agglomeration whereas in SEBS-SC-TiO_2 the dispersion is a mixture of agglomerations of different sizes. Despite of the presence PDMS shield on the TiO_2, the nanoparticles still tend to form agglomerations in solution cast films. Such agglomerations are commonly observed

in nanocomposites when the particle-particle interaction dominates the particle-matrix interactions. To overcome the former interactions, ultrasonication is commonly used. Due to the acoustic cavitation effect, sonication result in disruption of intra-molecular forces between nanoparticles for dispersing them finely in the polymer matrix. However, in SEBS-SC-TiO_2 the agglomeration still appears even after applying ultrasonication. This could be attributed to the processing method. Solution casting method is widely used for preparing films with equilibrium microstructure. It provides sufficient time for the disordered polymer chains and nanoparticles to relax from molecular level constrains and reach equilibrium state. During this process, the nanoparticles reorganize to form agglomerations due to stronger interaction between nanoparticle than that of particle and matrix. In contrast, the melt-mix samples appear to have a better dispersion. The enhancement in the dispersion in SEBS_MM_TiO_2could be attributed to the various parameters involved in the melt processing technique. One of the primary reasons is the mechanical shear force applied by the twin-screw extruder. In general, samples processed by twin-screw extruder undergo high shearing force to break the physical interactions between the particles in an agglomeration. In addition to shearing, the time involved in processing the samples into thin films is substantially low when compared to solution casting technique. Hence, the high speed processing with large shearing force could be the primary reason for the observed improvement in the dispersion of nanoparticles melt processed.

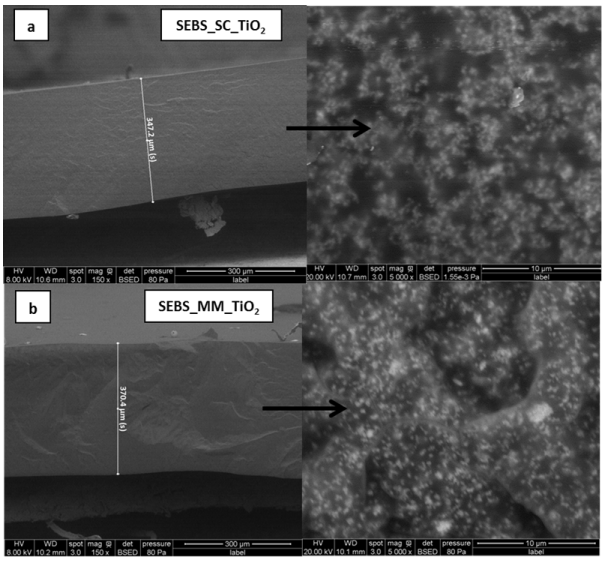

Figure 2.4: Fracture surface morphology of SEBS/TiO_2 nanocomposites, a) SEBS-SC-TiO_2, b) SEBS-MM-TiO_2

2.3.2 Permittivity

Table.I shows the results of performing the permittivity measurements described before. It can be seen that the melt-mixing process enhances the permittivity of the film even in the case of pure polymer with no nanoparticle added. However, this effect is noticed to have a higher impact in the case of the pure film rather than with the nanoparticles added. This might be due to the pressing process, which tends to produce films with higher density and fewer voids in the matrix, therefore the conductivity of the whole matrix is being enhanced hence leads to a higher permittivity.

Table 2.1: Permittivity Analysis

Sample	Permittivity
SEBS_SC	2.15
SEBS_MM	3.64
SEBS_SC_TiO_2	4.81
SEBS_MM_TiO_2	4.87

2.3.3 Thermogravimetric analysis (TGA)

The thermal stability of the nanocomposites SEBS-MM-TiO_2 and SEBS-SC-TiO_2 were investigated by thermogravimetric analysis (TGA) in atmospheric air. The influence of process induced dispersion of nanoparticles on the thermal stability of the samples can be studied from their respective TGA curves as shown in Figure 2. The samples appear to be stable with our decreasing up to 200 ^{o}C followed by an onset of degradation. The different stages involved in degradation of the investigated samples can be distinctly observed from the prominent peaks in the derivative weight % curves (Figure 2b). The thermal properties of pure SEBS studied previously by Xiaoyan *et al.* [20] reveals that the SEBS decomposes completely in a single stage starting at 378 ^{o}C and it chars completely at 475 ^{o}C. However, as the current samples are composed of poly-olefinic oil and TiO_2nanoparticles, we observe multiple degradation stages in the TGA curves of the SEBS nanocomposites. The primary (peak1) and secondary (peak2) peaks could be attributed to the degradation of the poly-olefinic oil and the SEBS phases respectively. The shoulder-like peak at high peak ˜450 ^{o}C might be from the complete degradation of the olefinic oil phase. The primary and secondary peaks were also observed to shift to high temperature in sample processed my melt mixing. The primary peak shifted from 289 to 310 ^{o}C and the secondary peak sifted from 369 to 392 ^{o}C. The shifts in the peak position could be revealed as the improvement in the resistance toward thermal degradation as a result if enhanced dispersion of nanoparticles in the nanocomposites. After complete degradation of the polymer matrix, the residual weight remaining above 450 ^{o}C corresponds to the wt.% of TiO_2 present in the samples. The residual weights of SEBS-MM-TiO_2 and SEBS-SC-$TiO_2$are 35 and 49 wt.% respectively. The difference in the concentration of TiO_2 indicates the existence of some losses during the mixing process, which need to be compensated.

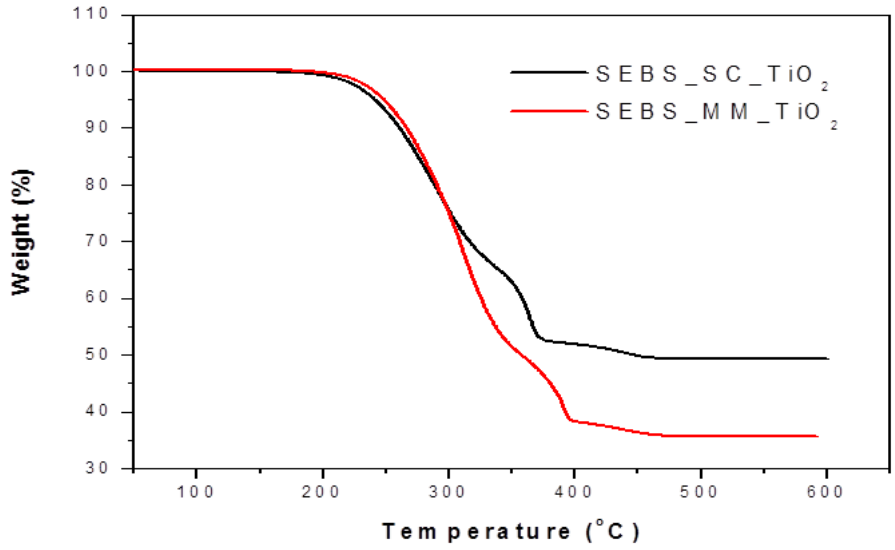

(a)

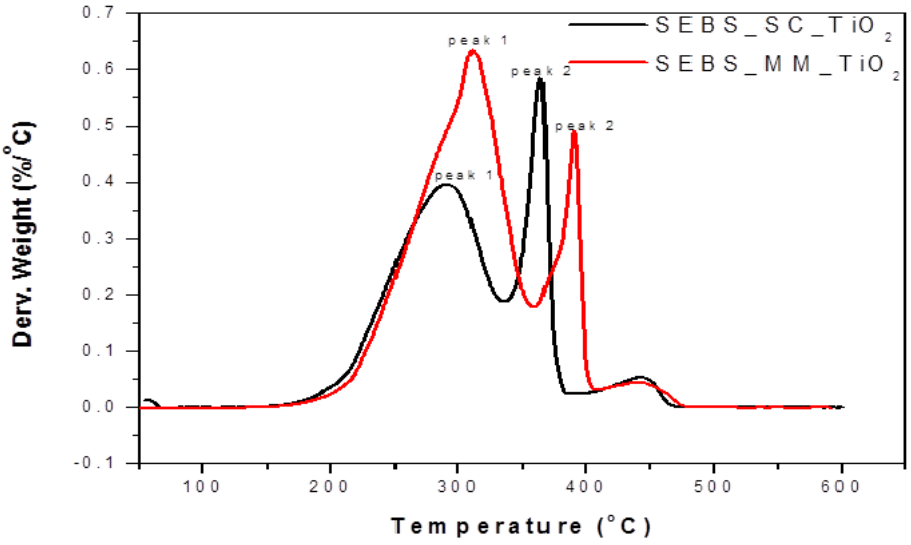

(b)

Figure 2.5: Thermogravimetric analysis results of SEBS nanocomposites. a) Weight % vs Temp. and b) Derv. Weight vs Temp

2.3.4 Mechanical properties

The engineering stress-strain curves of SEBS samples processed by solution cast and melt mixing methods with and without TiO_2 nanoparticles are shown in Figure. 2.6. The stress-strain profile of all the materials appear to show a soft elastomeric behavior with a low yield strength (< 0.5 MPa) followed by strain hardening (> 2 MPa) with a high elongation before break (> 1000 %). A significant influence of the processing method on the final tensile properties can be studied from Figure. 2.6. Over the entire strain axes, the samples processed by solution cast technique shows superior tensile strength then the melt processed counterpart. Whereas, the elongation at break for melt processed sample is higher than solution cast samples. In pure block copolymers, the physical and mechanical properties in the bulk material are primarily governed by their inherent nanostructure. Cast film technique is commonly used to achieve well-ordered equilibrium nanostructure, whereas melt processing results in a disordered phase structure.

In the present work, the observed deference in the mechanical properties between solutions cast and melt-mix process samples can be attributed to the change in the nanostructure

present in the post processed samples. Furthermore, with the addition of nano-filler, the melt processed sample shows a strong enhancement in the tensile strength when compare to the solution cast sample. The increase in the mechanical strength can be attributed to the high reinforcing efficiency of nanoparticles in melt processed samples. Generally, addition of rigid fillers in soft polymer results in improving the strength of the polymer due to interaction between the soft polymer chains with the rigid fillers. In the present samples, the enhancement in the dispersion after high-shear melt mixing methods (observed from SEM micrograph) resulted in increasing specific surface of interaction on the nanoparticle. However, in the solution cast samples, these interactions are limited due to the formation of microscopic agglomerations. As a final remark, it is worth noticing that, the observed difference in the wt.% of the TiO_2filler between SEBS-MM-TiO_2 and

SEBS-SC-$TiO_2$from TGA results make it difficult to study the influence of processing on the mechanical properties in the nanocomposites.

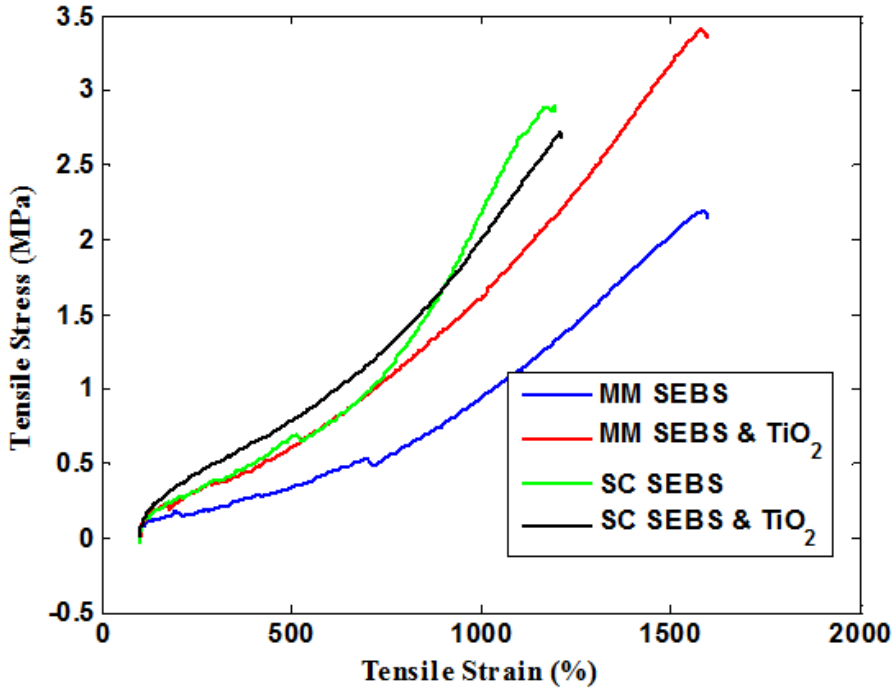

Figure 2.6: Stress-strain curves of SEBS-SC, SEBS-MM and their nanocomposites

2.4 Conclusion

In the this chapter,

- The polymer composite of SEBS and titanium dioxide (TiO_2) are used.
- The nanocomposite films are successfully produced by well-established high speed polymer processing techniques. The samples are fabricated by blending TiO_2 in SEBS by using high-shear melt mixing technique followed by converting the blend to thin films ($\sim 200\ \mu m$) by compression molding.
- The physical and mechanical properties of the melt processed samples were compared with the control samples prepared by cast film technique.

- The fracture surface analysis from scanning electron microscope (SEM) revealed a significant enhancement in the dispersion of nanoparticle after melt processing.
- The improvement in the dispersion increased the thermal stability of the nanocomposites as observed from the thermogravimetric analysis (TGA).
- The mechanical properties of the samples were measured by conducting tensile tests. As a result of fine dispersion of the nanoparticle, a strong reinforcing efficiency of nanoparticles was observed in melt processed samples when compared to the solution cast samples.
- These findings can lead to improved manufacturing processes for our soft capacitors, resulting in enhanced cost-effectiveness of the sensing method.

CHAPTER 3. MATERIAL OPTIMIZATION

The work in this chapter has been dessiminated in the Polymer journal in the publication

"INTERFACIAL TREATMENT EFFECTS ON BEHAVIOR OF SOFT NANO-COMPOSITES FOR HIGHLY STRETCHABLE DIELECTRICS"

3.1 Introduction

Deformable dielectrics are found in various applications and have been widely used to achieve high flexibility and stretchability [Yao and Zhu, 2014, Yan et al., 2014, Ho et al., 2013]. Dielectric materials with high energy density [Zeman, 2007] have also gained great attention for their transducing properties as they efficiently convert energy signals required for sensing, actuating, and energy harvesting [Shankar et al., 2008, Lipert et al., 2002]. Soft elastomeric dielectrics are vastly used in manufacturing of soft sensors and actuators, targeting several applications such as structural health monitoring by enabling skin-like sensing solutions [Laflamme et al., 2012], and advanced bionics where sensors and actuators are used interchangeably to create a substitute to human organs and to replace sensing elements and muscles. A sensors function is to convert input stimuli which can include mechanical, temperature change, and magnetic field. The performance of a sensor is inherently dependent on its mechanical and electrical properties. Polymers are very versatile materials, with an important potential for property alterations achieved through variations in polymerization chemistry, compounding and

processing [Nelson and Kutty, 2004]. By embedding fillers with high permittivity in a highly elastic polymer matrix, it is possible to create a stretchable sensor with enhanced sensitivity [Kollosche et al., 2011]. For this purpose, an elastomeric composite of poly-(styrene-ethylene-butylene-styrene (SEBS) block copolymer (BCP) filled with rutile titania (TiO_2) has been developed by the authors to fabricate a soft stretchable elastomeric sensor for structural health monitoring (SHM) of mesosystems [Ho et al., 2013, Zeman, 2007]. The proposed sensing application was for civil infrastructure [Laflamme et al., 2012], for which the monitored levels of strain are typically small [Laflamme et al., 2013b]. The choice of a BCP is motivated by the heterogeneous phase separation capabilities at the nanoscale [Ren et al., 2000,Krishnamoorti et al., 2001,Laurer et al., 1996]. BCPs have shown superior control on the spatial and orientational distribution of nanofillers used to alter their properties [Bockstaller et al., 2005][14]. Thermoplastic BCPs are physically cross-linked materials and enable broad range of processing techniques. In particular, SEBS is a soluble tri-BCP thermoplastic elastomer with a rubbery and semi-crystalline domain. It is used in many medical applications due to its purity, softness, elasticity, and strength [Yoda, 1998][15]. The inorganic TiO_2 particles (average size of 300nm) are characterized by a high anisotropic permittivity [Cava et al., 1995][16] of approximately 120 along the x axis. The composite is thought of as a host guest system where the SEBS provides the matrix to disperse filler particles, which show higher stiffness due to the presence of the filler. The interface between the filler and the polymer matrix of nanocomposites can have an important effect on its mechanical and electrical properties [Mc Carthy et al., 2009,Smith et al., 2008][17, 18]. The surface interaction between the filler and the polymeric matrix may also influence the dispersion process. In our case, the interaction between SEBS and TiO_2 is obstructed by the non-polar nature of SEBS, which prevents the polar inorganic TiO_2 particles form properly dispersing throughout the polymer matrix uniformly. To resolve this issue Ganguly et al. [Ganguly et al., 2006][19] proposed modifying the SEBS by grafting polar functional groups such as maleic anhydride, im-

proving the dispersion process. Stoyanov et al. [Kollosche et al., 2011][9], used silicone (PDMS, polydimethylsiloxane) oil-coated TiO_2 particles to enhance the particle matrix interaction and dispersability. The existence of the non-polar methyl (CH_3) end groups in the PDMS improves the affinity between the surfaces due to the non-polar nature of the SEBS matrix, thus enabling a more homogeneous distribution. The coated particles are used in this study. Research suggests that having higher interfacial surfaces leads to higher permittivity [Mc Carthy et al., 2009, Smith et al., 2008][17, 18], and has the potential to increase permittivity by up to 100 times [Dang et al., 2008, Huang et al., 2003, Panda et al., 2008, Wang and Dang, 2005][20-23]. In particular, for nanocomposites fabricated with TiO_2 [Mc Carthy et al., 2009] [17] and $BaTiO_3$ [Panda et al., 2008][22], researchers found that simple mixing rules applies and the experimental results matched the theoretical ones [Yoda, 1998, Cava et al., 1995, Bruggeman, 1935] [15,16][24]. At low levels, an increase in filler volume fraction leads to an increase in permittivity, but to a decrease in the breakdown strength by over 50Silane coupling agents can also be used to provide adhesion between surfaces. Salines are organofunctional groups capable of decreasing the interfacial tension. They bond inorganic material such as mineral fillers (TiO_2) to organic matrices such as (SEBS), and they provide adhesion between polar phase polymers and nonpolar fillers. Using Bis[3-(triethoxysilyl)propyl]tetra sulfide (Si-69), the $Si(OR)_3$ reacts with the polar components and the organofunctional group reacts with the nonpolar matrix [Nelson and Kutty, 2004][8]. Kaynak kaynak2003use[26] studied the effect of adding different types of silane coupling agents to an epoxy matrix filled with recycled rubber particles. Results showed that some of the silane coupling agents led to an increase in tensile strength, but also to a reduction in the impact and fracture toughness of the specimens. Ismail et al. [Ismail et al., 2002][27] used silane coupling agent Si-69 with natural rubber composite filled with bamboo fiber and investigated the effects on the mechanical properties and curing time. Results showed an increase in the tensile strength, tear strength, hardness and tensile modulus. The fabrication process

may also influence the mechanical and dielectric properties of polymer composites. Recently we reported the advantages of melt mixing on solution mixing for the fabrication of soft dielectrics [Saleem et al., 2013][28]. We showed that the melt mixing process enables 1) faster fabrication because of the solvent-free process that does not require evaporation time, 2) enhanced control over the membranes size and thickness, 3) easier processing of large quantities 4) a fine dispersion of the filler material due to high shear mixing, and 5) the elimination of organic solvent within the nanocomposite that exists when a solution cast process is used, which could influence mechanical and dielectric properties of the composite. The objective of this chapter is to study the influence of molecular level interaction between the filler particles and polymer matrix to enable soft dielectrics with enhanced sensing and actuation properties. Here, we investigate the effect of interfacial treatment on SEBS-TiO_2 nanocomposites fabricated using a melt mixing process. The morphology, mechanical properties, and dielectric properties are studied in function of treatment, including PDMS silicone oil and Si-69 coupling agent.

3.1.1 Sample preparation

Four types of samples were prepared, all using the melt mixing method described in chapter 2, a pure SEBS, SEBS filled with uncoated TiO_2 particles, SEBS filled with uncoated TiO_2 particles using Si-69, and SEBS filled with PDMS oil coated TiO_2 particles. All samples have filler content of 15 vol% of SEBS. Table. 1 shows the sample composition as well as their designation.

Table 3.1: Samples designation and filler

Name	Polymer matrix	Filler (15 vol%)
Pure SEBS	SEBS	none
SEBS_ TiO_2	SEBS	Uncoated TiO_2
SEBS_ TiO2 (PDMS)	SEBS	TiO_2 particles coated with PDMS oil
SEBS_ TiO2 (Si-69)	SEBS	Uncoated TiO_2 + Si-69

3.2 Experimental

3.2.1 Characterization of morphology, thermal and mechanical properties

The morphology of the composites was characterized using an FEI Quanta 250-FEG scanning electron microscopy (SEM) under 80 Pa of water vapor. The SEM images were acquired by an accelerating voltage of 8 kV. Fresh sample surfaces were obtained by cryo-fracturing the nanocomposite films after freezing with liquid nitrogen (LN_2). The samples were taken from randomly selected places from the films. Two samples were taken from each of the four specimens. The fractured surfaces were sputtered with iridium to enhance electrons emission and reduce sample charging.

The dynamic mechanical properties and glass transition temperature of samples of dimension 20×8×0.2 mm^3 were obtained using a dynamic mechanical analysis (DMA) Q-800 from TA Instruments (New Castle, DE). The DMA test was conducted in tensile mode using tensile film clamps. Temperature sweep tests were carried out between -100 to 60 ^{O}C at 1 Hz frequency, strain amplitude of 40 mm, and a heating rate of 3°C/min. The elastic storage modulus (E') and damping coefficient (tan δ) were recorded over the temperature range. Thermogravimetric analysis (TGA) using a TGA-Q50 from TA Instruments was conducted to study the thermal stability and the residual wt.% of the samples. Tests are performed for temperatures ranging from ambient to 600 °C at a

heating rate of 10 °C/min. An Instron universal testing machine (model 5569) with a ±10 N load cell is used to perform the tensile tests until rupture in an ambient temperature at a speed of 50 mm/min, selected lower than the minimum required by ASTM D412-06a for higher accuracy. The tensile tests were conducted on 30 mm dog-bone sample shaped according to ISO 527 type 5A.

3.2.2 Dielectric spectroscopy

The dielectric properties were measured under ambient temperature conditions using a Novocontrol dielectric spectrometer (Novocontrol Technologies GmbH & Co. KG). A circular specimen of the dielectric with diameter of 20mm was punched out and sandwiched between two copper electrodes (20 mm diameter). Frequency depended real and imaginary part of the permittivity were measured in the interval 1 Hz to 1 MHz.

3.3 Results and Discussion

3.3.1 Morphology

Figure. 3.1 shows the SEM images from cryo-fractured surfaces of the samples listed in Table. 3.1 Images show fine dispersion in all of the samples with fillers. However, the fractured surface morphology of the specimen with PDMS-coated TiO_2 particles appears to have a slightly more homogenous structure with fewer gaps. Minor agglomerations are found in the samples with the uncoated filler and the PDMS coated filler. Similar agglomerations are found in composites when the particle-particle interactions dominate the particle-matrix interactions. The low particle density areas with non-uniform dispersion of the filler seen in Figure. 2b and 2d (indicated by dotted circles) may be caused by softening of the polymer phase present under the SEM electron beams in various modes (low or high vacuum).

Good dispersion results may be attributed to the high shearing forces applied in

the twin melt mixer that may have broken the particle-particle interaction forming the agglomerations, resulting in enhanced matrix-particle interaction and more homogenous matrices.

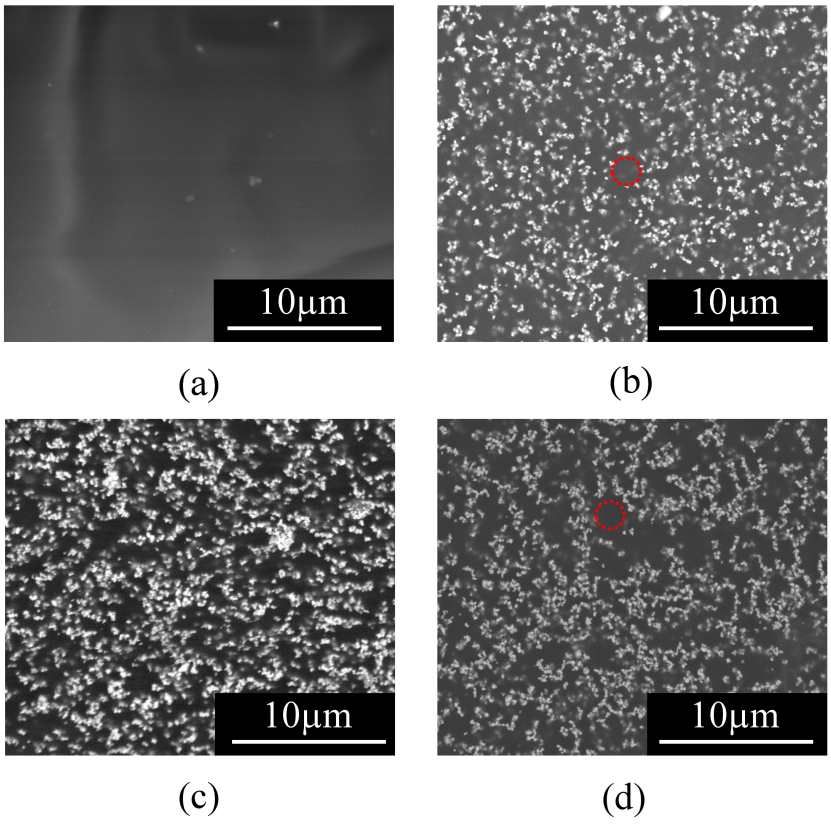

Figure 3.1: SEM images of a) pure SEBS, b) SEBS-TiO2, c) SEBS-TiO2 (PDMS) and d) SEBS-TiO2 (Si-69). The dotted red circle shows areas with lower density of filler.

3.3.2 Dynamic mechanical analysis

The dynamic mechanical storage modulus (G') and damping coefficient (tan δ) was used to characterize the change in the phase behavior and modulus of the polymer composite over a broad range of temperatures. Figure. 3.2a and 3.2b show the temperature dependence of G' and tan δ of the specimens. All filled specimens have similar behavior with a glassy plateau extended between -100 ^{o}C to -60 ^{o}C, followed by a glass transition

(T_g) and a rubbery plateau. In the glassy regime, the modulus of the material increased from 940 MPa to 2000-3000 MPa after blending with the fillers. A nominal difference in the modulus can be observed in the nanocomposite.

The glass transition temperature (T_g) of the materials can be identified from the position of the peak of tan δ. The addition of TiO_2 in the SEBS does not show a significant shift in T_g. Surface modification of TiO_2 and addition of Si-69 show negligible effects on the peak position of the tan δ curves. However, a reduction in the peak intensity can be observed for SEBS- TiO_2(PDMS) samples. As the peak intensity of tan δ curves is directly proportional to the damping ability or softness of the material, the reduction in peak intensity indicates a strong reinforcing efficiency with PDMS modified TiO_2 particles. Beyond T_g, the modulus of the pure SEBS sample declines completely and the sample fails at small strain. This is attributed to the terminal response that is commonly observed in thermoplastic homopolymer. Whereas, all the composite samples depict a nonterminal response with a plateau behavior in the G' curve. The temperature-dependent non-terminal response in polymers is associated with either physical or chemical interactions present within the material that can limit the flow behavior of the material. In the investigated composites, a strong physical interaction between the filler particles and polymer matrix is responsible for the observed non-terminal response. However, as si-69 is less stable at elevated temperatures, SEBS with si-69 is showing lower G' curve in the rubbery regime.

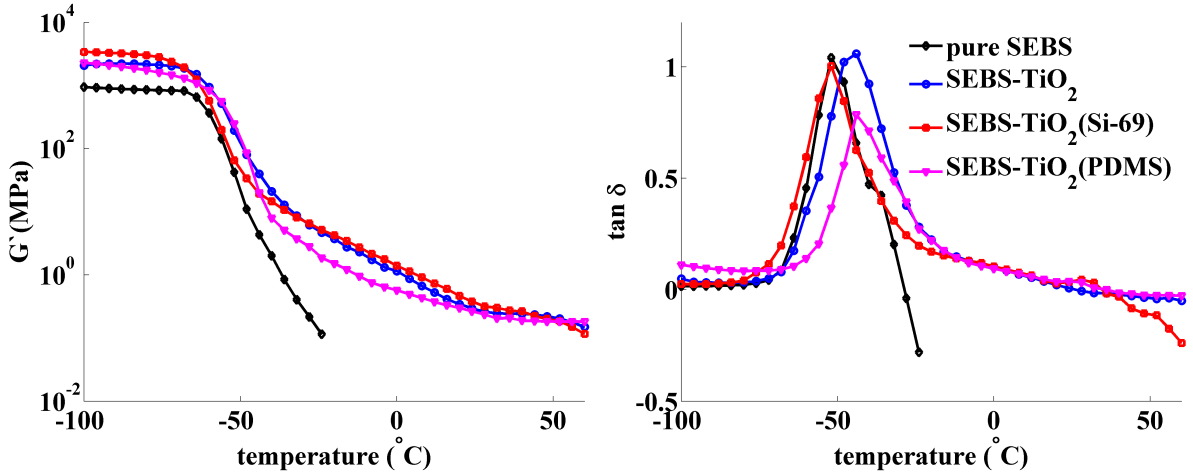

(a) (b)

Figure 3.2: a) Storage modulus recorded at different temperatures, and b) Damping coefficient recorded at different temperatures

3.3.3 Mechanical analysis

The tensile stress-strain curves for all specimens are shown in Figure. 3.3 The stress-strain profile shows a soft elastomeric behavior with a low yield strength followed by strain hardening. Pure SEBS and SEBS with coated TiO_2 have similar stress-strain behavior with high tensile stress and strain at break. The addition of the coated TiO_2 particles (SEBS-TiO_2(PDMS)) shows an increase the ductility of the pure elastomer with a high elongation before break (900%), whereas uncoated TiO_2 and TiO_2 with coupling agent(Si-69) reveal a reduction in strength, and a smaller elongation after break (˜30% reduction). The sample with coated TiO_2 particles exhibits ductility similar to the pure SEBS, which can be attributed to the plasticizing effect caused by the soft PDMS coating. Conversely, the modulus of the specimens measured at low strains is higher for SEBS-TiO_2 and SEBS-TiO_2(Si-69) when compared to pure SEBS and SEBS with PDMS coated nanoparticles. The mechanical behavior of the SEBS-TiO_2 sample appears to remain linear until break. The stiffness of each specimen is determined by fitting the

Hooke model to the first 5% stress strain data. Young's modulus measured below 5% strain is listed in Table. 3.2 and the blow up of this region is shown in Figure.3.3 In pure block copolymers, the physical and mechanical properties in the bulk material are primarily governed by their inherent nanostructure. Here the observed difference in the modulus between the four samples can be attributed to the change in the nanostructure present in the post processed samples in presence of nanofillers. Generally, the addition of rigid fillers in soft polymers results in an increase of the modulus.

The dispersed filler act as rigid bodies constraining the deformation of the soft SEBS matrix and increasing the Young's modulus. However, the enhancement in the modulus is primarily controlled by the dispersion of the particles. As the SEM images (Figure. 3.1) reveal fine dispersion of nanoparticles in all the samples, the observed difference might be coming from the fabrication of the nanocomposites. In SEBS-TiO2 and SEBS-TiO2 (Si-69) samples, the direct interaction between the SEBS and TiO_2 phases result in enhanced material stiffness.

Table 3.2: Initial Youngs modulus of specimens

Sample	pure SEBS	SEBS-TiO_2	SEBS-TiO_2(Si-69)	SEBS-TiO_2(PDMS)
Modulus (MPa)	0.46	0.57	0.91	0.77

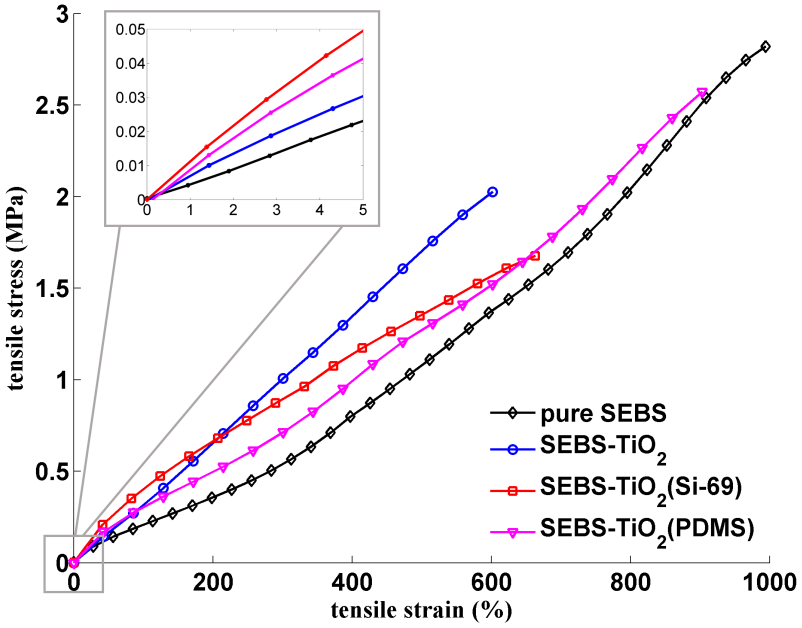

Figure 3.3: Stress-strain curves of all tested samples

3.3.4 Thermogravimetric analysis

TGA was conducted to identify the quantity of TiO_2 left in the samples after melt processing and to investigate the thermal stability of the nanocomposites. Results are shown in Figure. 3.4. All the composites (Figure. 3.1) appear to have the same amount of TiO_2 after complete degradation of the SEBS as observed from the residual weight between 500 to 600 ^oC. This level ($\sim$ 45 wt.% which converts to 15 vol.%) is consistent with the prepared 15 vol.% of TiO_2. Figure. 3.4 also provides information about the influence of blending TiO_2 with various modifications on the thermal stability of the polymer matrix. Specimens with PDMS coating exhibit a higher stability with respect to others.

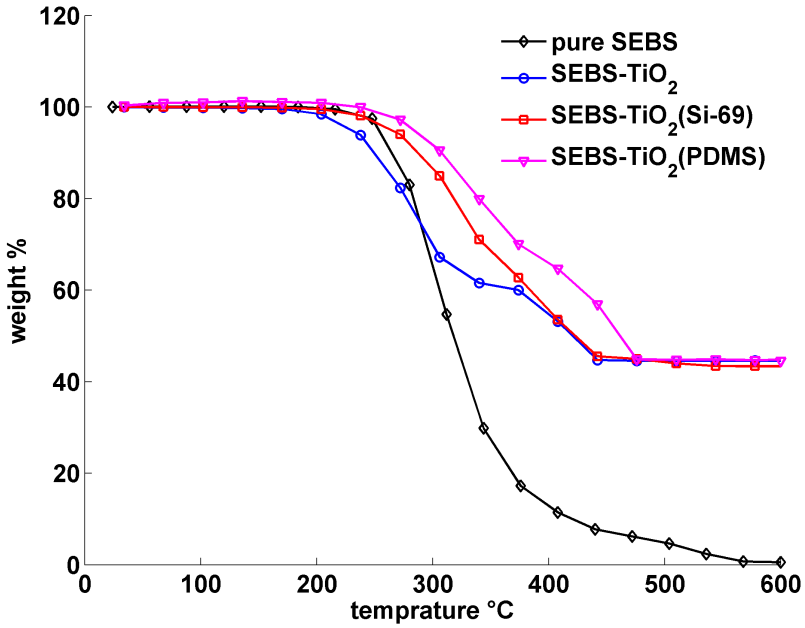

Figure 3.4: TGA analysis results

3.3.5 Dielectric analysis

The dielectric relaxation spectroscopy of the pure elastomer and all composites are shown in Figure. 3.6a and 3.6b. Results exhibit an increase in the permittivity of specimens with filler content over the whole frequency range. For the pure SEBS, we notice a nearly frequency independent behavior of the permittivity with a value of 2.1 and low dielectric losses (Table. 3.3). The addition of the TiO_2 led to a substantial increase in the permittivity and a significant shift to higher losses. For uncoated TiO_2, the permittivity was 3.8 at 100 Hz, approximately twice of the value for pure SEBS, with noticeable frequency dependence below 100 Hz.

The addition of coated particles has a similar effect, but with an improved stability of the permittivity with respect to frequency. The loss tangent (tan δ) increases with the addition of fillers. The PDMS-coated TiO_2 appears to further increase tan δ, while the Si-69 coating decreases tan δ. The uncoated particles have the maximum damping coeffi-

cient among all. The comparison to classic dielectric mixing rules using the Bruggemann and Lichtenegger models [Bruggeman, 1935] (shown in Figure. 3.5) yields a permittivity of 3.8, which agrees with the permittivity of the SEBS-TiO_2 specimen measured using dielectric spectroscopy. The dielectric analysis also demonstrated that the composite permittivity with coated particles was slightly decreased, yet comparable. The slight reduction in the measured permittivity for SEBS-TiO_2(Si-69) and SEBS-TiO_2(PDMS) can be attributed to the treatment used in the process that affected the overall permittivity of the nanocomposite. From the morphology analysis, results showed that the use of coated particles resulted in a better dispersion than with the coupling agent. The use of si-69 also resulted in a decrease in permittivity of approximately 10.5% compared with the use of uncoated particles. This notable decrease in permittivity can be explained by a change in the interphase properties of the SEBS/TiO_2 composite. Similar results were concluded from a study conducted by McCarthy [Mc Carthy et al., 2009].

Table 3.3: Relative permittivity (taken at 100 Hz)

Sample	pure SEBS	SEBS-TiO_2	SEBS-TiO_2(Si-69)	SEBS-TiO_2(PDMS)
Relative permittivity	2.1	3.8	3.4	3.7
Dielectric Loss (tan δ)	0.0004	0.0096	0.0023	0.004

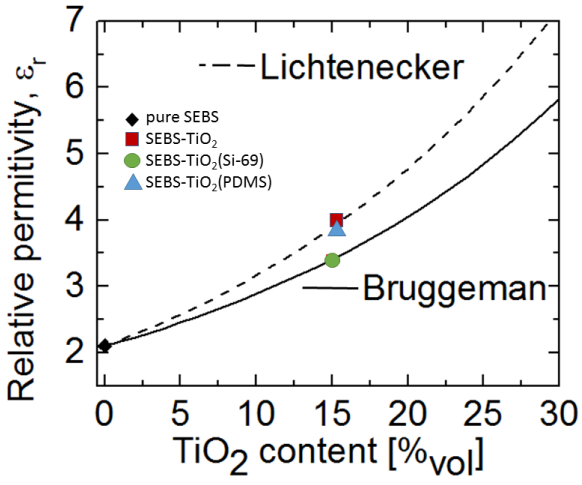

Figure 3.5: Comparison of eperimental and theoritical permitivitty

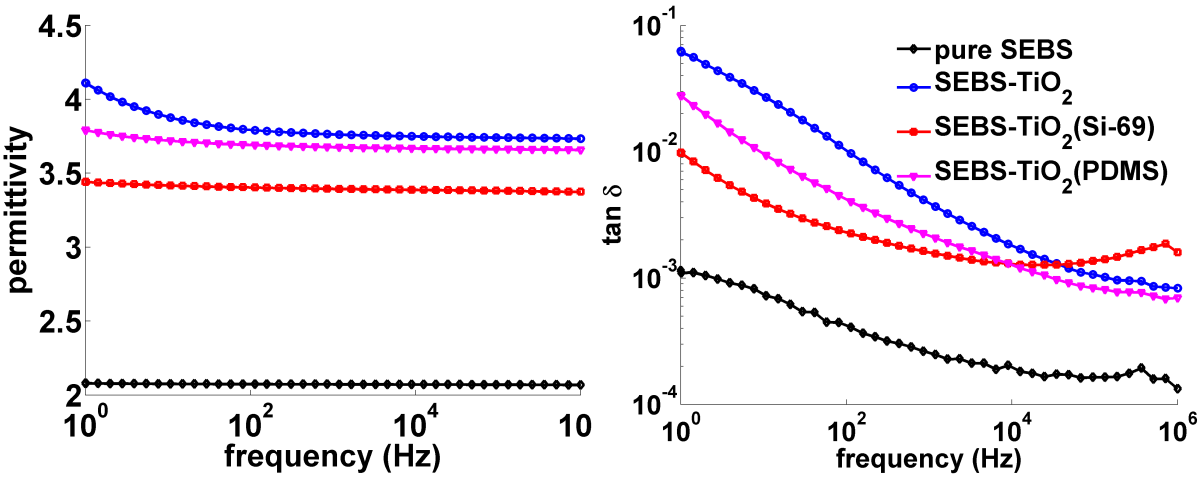

(a) (b)

Figure 3.6: a) Relative permitivitty, and b) loss coefficient recorded at different frequencies

3.4 Conclusions

- The interfacial influence of TiO_2 and SEBS for melt mixed nanocomposite dielectrics is studied.

- Uncoated TiO_2 has been compared with surface-treated TiO_2, and with a Si-69 enhanced SEBS solution.

- Morphology, mechanical, thermogravimetric, dynamic mechanical and dielectric analyses were conducted on the prepared samples.

- The results show that the samples filled with PDMS oil coated particles had superior performance in terms of stiffness where we had 67% increase, stretchability up to 900% before failure and permittivity enhancement by 45% after adding the filler with a small adverse effect observed using the treated filler particles.

- Melt mixing technique used for processing soft, stain sensitive sensors enables producing (soft dielectric with high energy density) sensors with uniform profile properties without involving organic solvent.

CHAPTER 4. SEC CHARACTERIZATION

The work in this chapter has been submitted to the materials evaluation in the American Society of Non-destructive Testing journal in the publication

"INVESTIGATION OF DYNAMIC PROPERTIES OF A NOVEL CAPACITIVE-BASED SENSING SKIN FOR NONDESTRUCTIVE EVALUATION"

4.1 Introduction

As mentioned before, the SEC is intended to be used in a network configuration for SHM applications. Structural systems are exposed to several types of loads including dead, live, wind and earthquake loads. These load can be classified into two main categories, static and dynamic. Therefore, to accurately predict the behavior of any structure, the monitoring system need to be capable to work in both the static and the dynamic modes. In this chapter, the static and the dynamic characteristics of the SEC are explored to check the capability of the SEC to be used in a SHM system. Linearity, sensitivity and dynamic measurements capability are properties to be investigated.

Recent investigations have been conducted on the characterization of the dynamic behavior of the SEC [Laflamme et al., 2014], with applications to monitoring of vibration signatures [Ubertini et al., 2014]. Both studies concluded that while the sensor can detect a change in dynamic properties, it only provides a linear response for mechanical excitations up to 15 Hz. It is hypothesized that a possible source of nonlinearity arises from a non-negligible frequency-dependence of the SEBS's Poisson ratio due to its

viscoelasticity [Tschoegl et al., 2002, Pritz, 2007, Kugler et al., 1990, Wada et al., 1962]. This chapter further investigates the dynamic response of the SEC for a wider range of excitation, considering mechanical frequencies up to 40 Hz, which covers a wide range of structural dynamics found in mesosystems. In this chapter an augmented electromechanical model that accommodates for possible sources of nonlinearity beyond 15 Hz is developed to enable SHM applications up to 40 Hz, a range covering the vast majority of the dominating frequency responses of civil infrastructures.

4.2 Static Characterization

4.2.1 Experiment

Two experiments are built to for the purpose of static characterization of the SEC. First a uniaxial experiment is done. The test setup consists of a simply supported aluminum plate of dimensions 440 $\times$ 116 $\times$ 6.4 mm^3 subjected to a three-point load setup to provide a constant strain field across the SEC. Note in all the experiments the monitored surface is sanded, painted with a primer, and a thin layer of an off-the-shelf epoxy (JB Kwik) is applied on which the sensors are adhered. The performance of the SEC is compared against an off the shelf resistive strain gauge (RSG) (Vishay Micro-Measurements, CEA-06-500UW-120) of resolution 1 $\mu\epsilon$. Both sensors are mounted onto the bottom surface of the plate, in the center, as shown in Figure. 4.1. The load is applied using a hand operated hydraulic test system (Enerpac) for the static tests, and a servo-hydraulic fatigue testing machine (MTS) for quasi-static tests. All tests are repeated three times. Data from the SECs are acquired using an inexpensive offthe-shelf data acquisition system (ACAM PCap01) sampled at 95.4 Hz. The SEC readings are compared against RSG with resolution of 1 $\mu\epsilon$ (Vishay Micro-Measurements, CEA-06-500UW-120). Strain gauge data are acquired using a Hewlett-Packard 3852 data acquisition system, and data sampled at 1.7 Hz when using the hand hydraulic, and 55

Hz when using the MTS. Data are filtered using a low-pass filter, and zeroed using the average capacitance while the beam is unloaded.

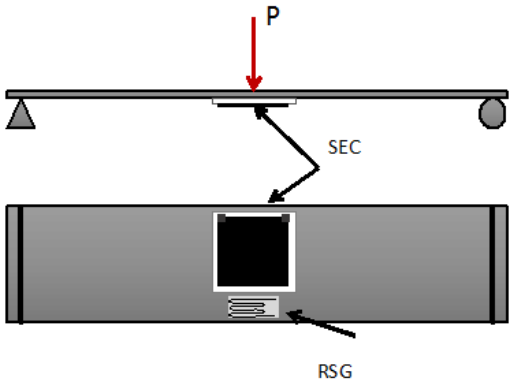

Figure 4.1: Schematic of the experimental setup for a single SEC

4.2.2 Results and discussion

A single SEC is first validated using a step load. Figure. 4.2 is a plot of the results in which the capacitance signal has been transformed into strain using Eqn. 4.6. The SEC signal raises above noise beyond 25 $\mu\epsilon$, but for strain levels above 55 $\mu\epsilon$, there is a constant difference of approximately 8 $\mu\epsilon$. Figure. 4.3 shows the results from a typical quasi-static load test. The excitation history consists of a displacement-based triangular wave loads with increasing frequencies from 0.0167 to 0.40 Hz.

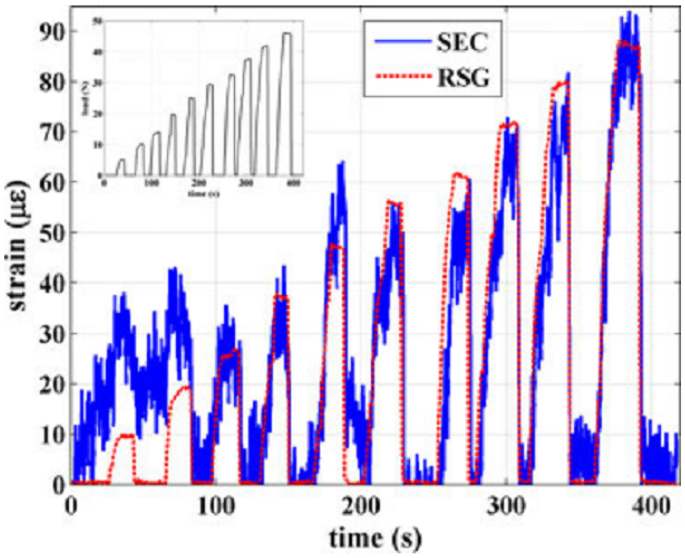

Figure 4.2: Strain history of an SEC versus RSG (step load).

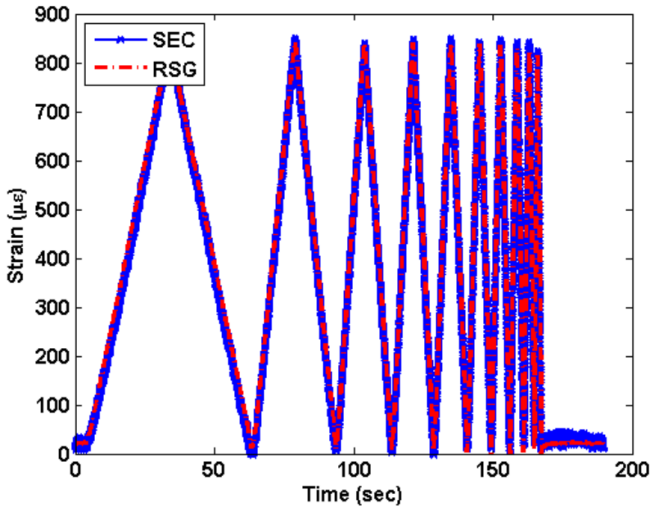

Figure 4.3: Strain history of an SEC versus RSG (triangular load) and actuator displacement.

Results show that the SEC is capable of tracking a quasi-static strain history within a given level of resolution. Figure. 4.4 is a plot of the SEC readings in function of the strain measured by the RSG, validating the linearity of the sensor. Its measured sensitivity is in agreement with the electromechanical model assuming the Poisson ratio

for aluminum is 0.3 and the $\varepsilon_y = \nu_{aluminum} \times \varepsilon_x$. Given that the dielectric permittivity does not change significantly in the low-frequency range (less than 100 Hz) [Stoyanov et al., 2011], a large portion of the measurement errors in both Figures 4.2 and 4.3 can be attributed to the electronics. First, there is a parasitic capacitance in the cables connecting to the sensors, which causes variations in the measured capacitance. Because SECs require very small power, this noise can be minimized by digitizing the signal at the source, enabling long distance transmissions, either over a wired or wireless link, with essentially no signal degradation. Second, the DAQ itself may not have the sufficient resolution for measuring small changes in capacitance.Other sources of error may come from imperfections in the sensor fabrication and geometry.

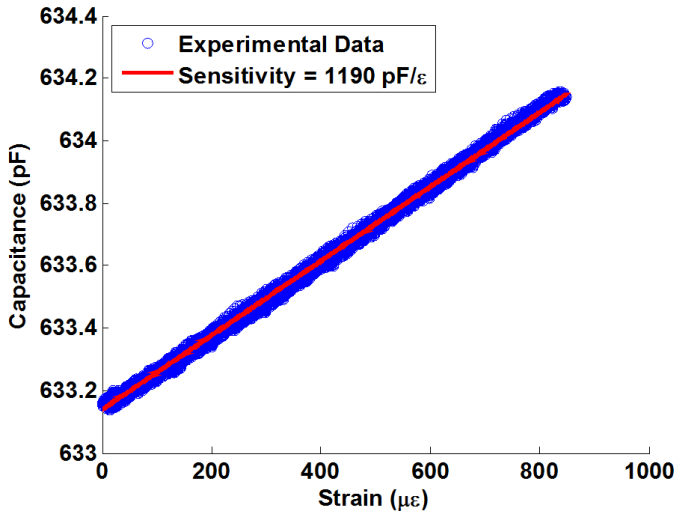

Figure 4.4: Sensitivity of the SEC in the quasi-static mode.

The second experimental setup for the quasi-static load test consists of six SECs deployed on a cantilever fiberglass plate of dimensions of dimensions 416 × 324 × 4 mm^3. The number of sensors is limited by the capacity of the data acquisition system used herein to read the SEC signals. Resistive strain gauges (RSGs) of 1 $\mu\varepsilon$ resolution (Vishay Micro-Measurements, CEA-06-500UW-120) are deployed around each SEC to benchmark the results. Two load configurations are investigated at the free edge: 1)

at the center; and 2) at the corner (top-right in Fig. 4.12). Data from the SECs are acquired using an off-the-shelf data acquisition system (ACAM PCap01) recorded at 20 Hz. Data from the RGSs are measured using a Hewlett-Packard 2850 data acquisition system at a sampling frequency of 1.7Hz. Fig. 4.5 shows the experimental setup.

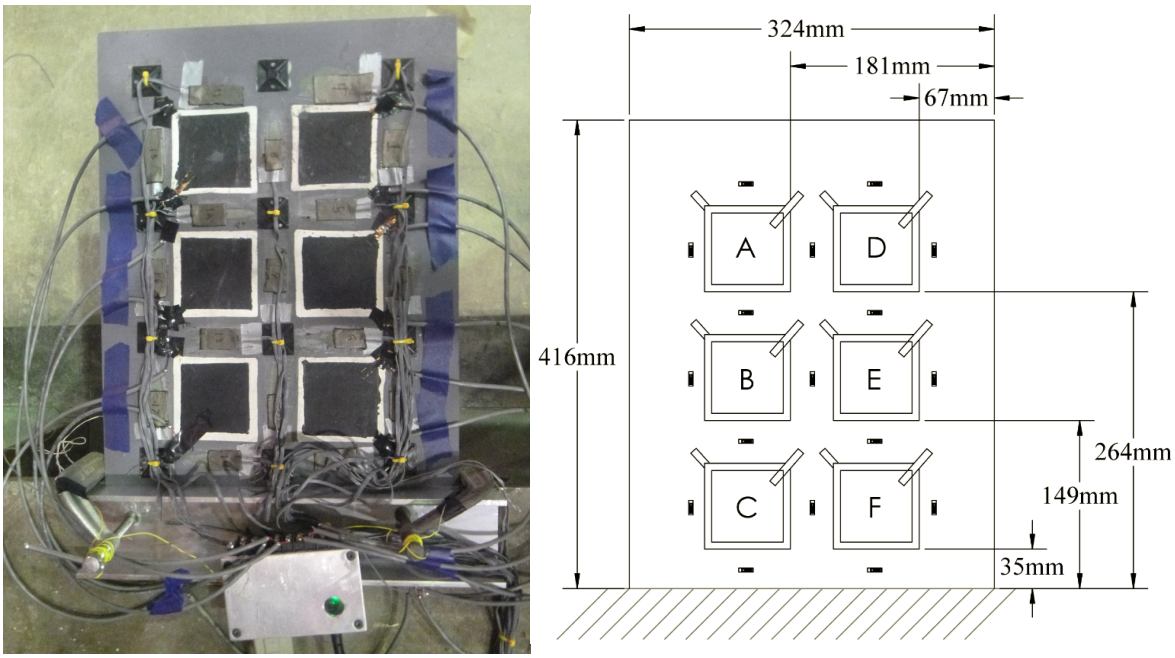

Figure 4.5: Quasi-static test setup

Fig.4.6 shows the time series results for the recorded additive strain from the SECs and RSGs. The additive strain from the SECs is directly obtained from Eq. 4.6, and compared against the average additive measurements of the RSGs surrounding the SECs. Plots show five distinct plateaus of strain. The first three plateaus are used for sensor calibration, and the fourth and fifth plateaus represent results from the center and the corner loads, respectively. SECs A and D exhibit a higher variance with respect to other SECs, which can be explained by the lower level of strain resulting in a higher noise-to-signal ratio. Note that it was reported earlier that the accuracy of an SEC in this particular measurement configuration is 25 $\mu\varepsilon$ [Laflamme et al., 2013a]. Results show good agreement between the SECs strain readings, obtained from the electromechanical

model, and the RSGs.

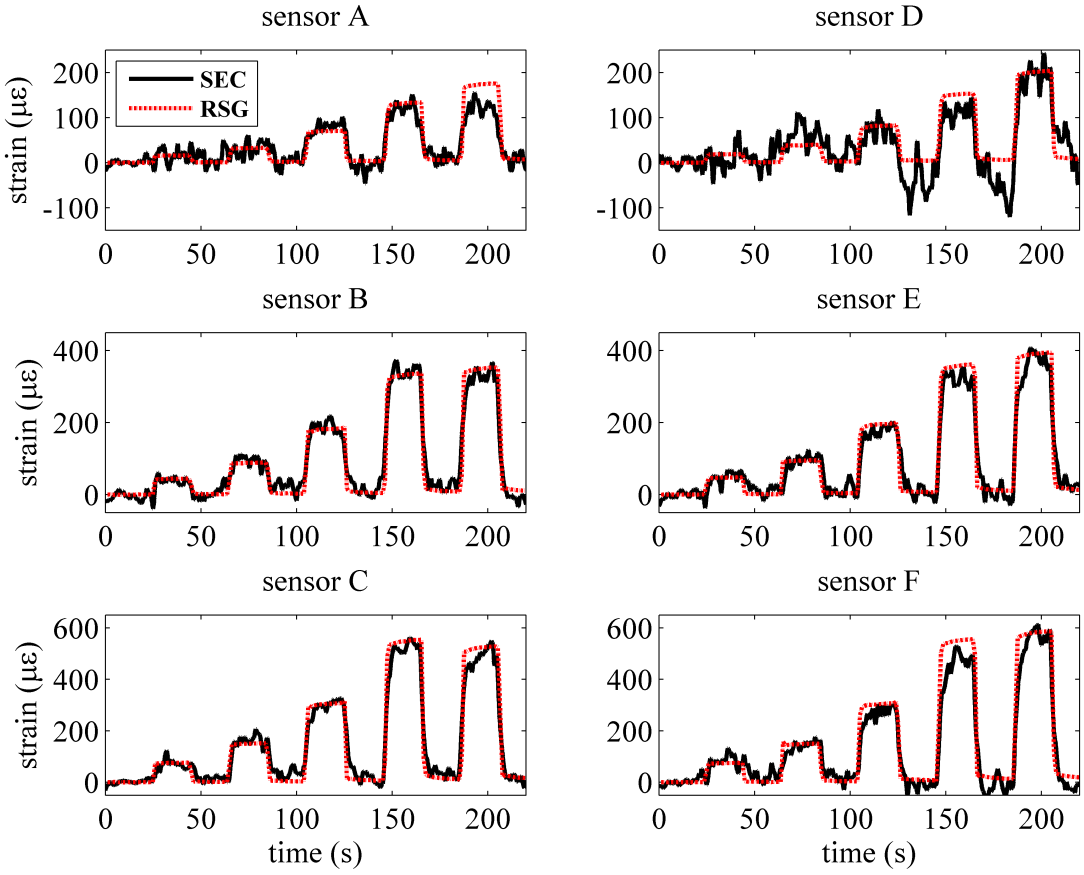

Figure 4.6: Static test results

4.3 Dynamic Characterization

In this section, the behavior of the SEC is investigated in the frequency range 1-40 Hz. Response linearity and sensitivity as a function of a frequency-dependent Poisson's ratio are studied. Finally, an augmented electromechanical model where ν is allowed to be frequency-dependent in Eq. (4.7) is presented.

4.3.1 Methodology

The test setup is shown in Fig. 4.7(a). It consists of an aluminum plate of dimensions 432 x 102 x 0.68 mm^3 excited axially, onto which an SEC is adhered. Two resistive strain gauges (RSGs) are installed onto the back of the plate opposite to the SEC, measuring strain in both the x and y directions independently, where x denotes the direction of the applied load and y is transverse to the load and in-plane with the SEC. Data from the SEC are recorded using an off-the-shelf DAQ (ACAM PCAP-02) at a sampling rate of 250 Hz.

The axial excitation is provided by a servo-hydraulic testing machine, and consists of a time-varying harmonic tensile force sweeping from 1 to 40 Hz in 1 Hz increments. The strain time history is shown in Figure 4.7(b). Due to equipment limitations, the displacement decreased with increasing frequency as it is observed in Figure 4.7(b).

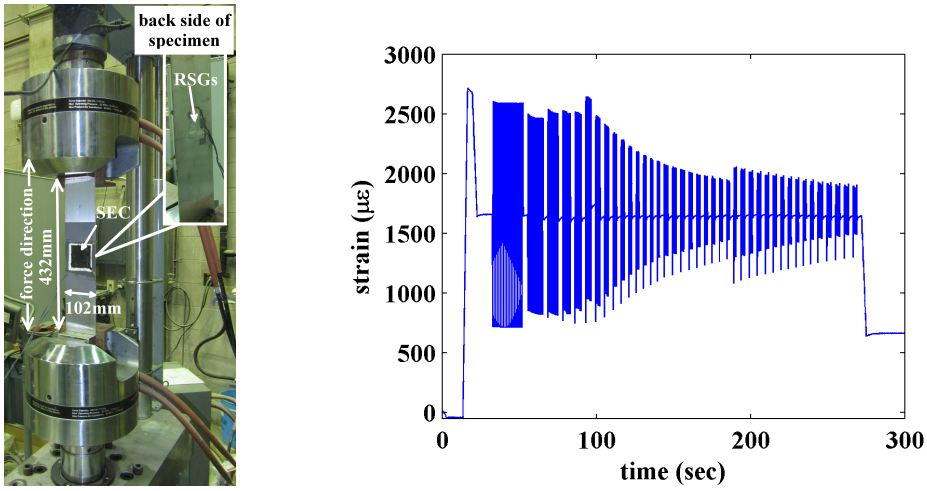

(a) (b)

Figure 4.7: a) Test setup and b) RSG strain data

Parameters of interest in the study of the dynamic behavior of the SEC are the linearity of the response and the gauge factor as a function of the excitation frequency. For each frequency of interest, the time histories of both the load input and the sensor's capacitance output were extracted using a window function. A band-pass filter designed

around this frequency was applied to both time series (input and output) to reduce noise. The linearity was assessed by plotting the filtered output versus the filtered input, and the experimental gauge factor back-calculated from Eq. 4.6 using the measured ε_x and ε_y from the resistive strain gauges and ΔC.

Figure 4.8 shows the filtered time series following this methodology at three particular frequencies: 1, 20 and 40 Hz, which represent the lowest, middle and highest frequencies in the sweep. A salient feature in the plots is the increase in the level of noise with the increase in frequency. This can be attributed to electromagnetic interference (EMI), despite careful attention to minimize such noise in the experimental setup (e.g., by utilizing shielded cables and grounding of components).

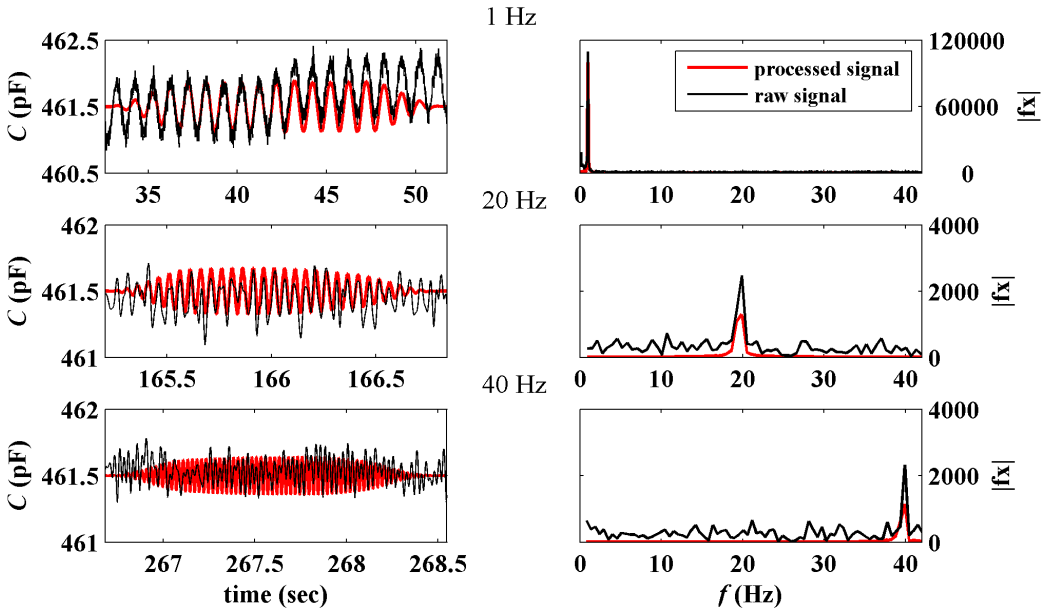

Figure 4.8: Time histories and Fourier transforms of signals provided by RSGs and SEC in the harmonic tensile load test

Figure 4.9 shows the wavelet transform of the raw signal (Figure 4.9(a)) compared against the processed signal (Figure 4.9(b)), using morlet wavelets. The wavelet transform is normalized at each discrete time interval to the highest wavelet amplitude. The black line is the input frequency content. Results validate the signal processing method-

ology, and show good agreement between the dynamic input and sensor output across the entire frequency range from 1 to 40 Hz.

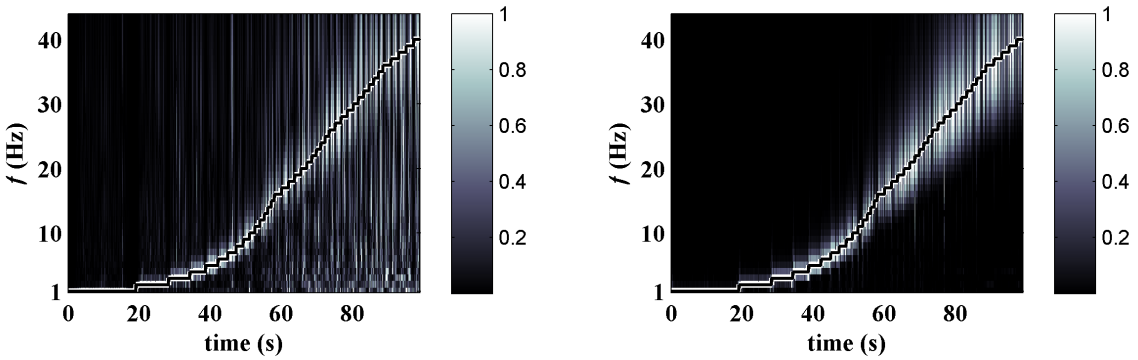

(a) (b)

Figure 4.9: Wavelet transform of the a) raw and the b) processed data

4.3.2 Results and discussion

The sensor linearity and sensitivity are studied through the investigation of the sensor's response as a function of frequencies. Figure 4.10 are plots of the response of the SEC against the measured additive strain $\varepsilon_x + \varepsilon_y$. The red line is the linear fit obtained via linear regression. The quality of the linear fit represents the linearity of the sensor, while the slope of the regression represents its sensitivity $S = \Delta C/(\varepsilon_x + \varepsilon_y)$. The root means square error (RMSE) is used as a performance measure for linearity, plotted in Fig. 4.11. The figure shows higher error at lower frequency excitations. This could be attributed to the higher magnitude of the strain input at lower frequencies. Yet, the overall RMSE shows a good linearity of the sensor.

Results from Fig. 4.10 show a decrease in sensitivity with increasing frequency. This can also be observed in a plot of the gauge factor calculated from the experimental results, shown in Figure 4.12. A two-term power series provided the best fit of the experimental gauge factor data. This fit illustrates the apparent reduction in the gauge factor as the frequency increases. The sensitivity S is reduced by 2.9% at 20 Hz and 11.5% at 40

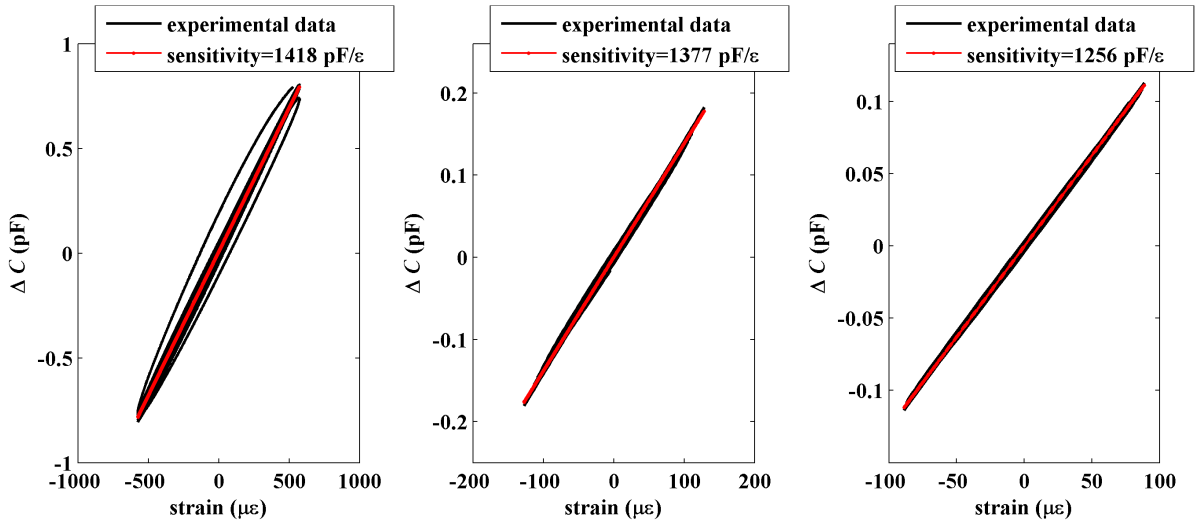

(a) (b) (c)

Figure 4.10: Sensitivity and linearity of the sensor signal at: a) 1 Hz; b) 20 Hz; and c) 40 Hz

Hz with respect to the reference S at 1 Hz as shown in Figures 4.10a, 4.10b, and 4.10c respectively.

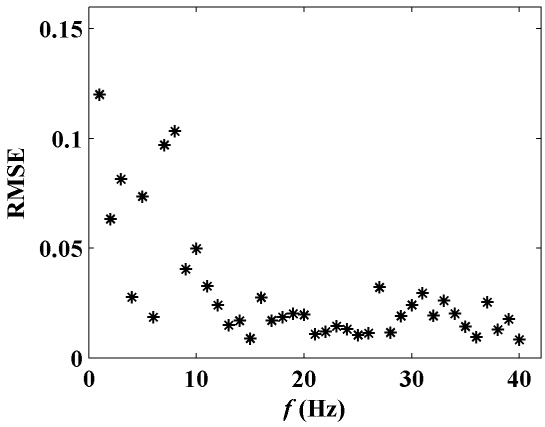

Figure 4.11: Root mean square fitting error for the capacitance data

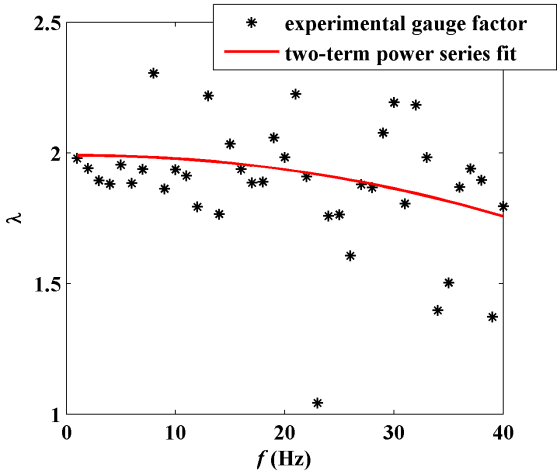

Figure 4.12: Experimental gauge factor

As explained in the introduction, we model the change in the sensor's sensitivity assuming that it can be explained by the complex Poisson's ratio of the material. Consider the strain modeled as a complex component [Pritz, 2007]:

$$\begin{aligned} \varepsilon_x(t) &= \hat{\varepsilon}_x e^{j\omega t} \\ \varepsilon_y(t) &= \hat{\varepsilon}_y e^{j\omega(t-\Delta t)} = \hat{\varepsilon}_y e^{j(\omega t - \delta_\nu)} \end{aligned} \tag{4.1}$$

where t is the time, $\hat{\varepsilon}_x$ is the amplitude of the axial strain, $\hat{\varepsilon}_y$ is the amplitude of the lateral strain modeled with the same frequency response as $\hat{\varepsilon}_x$, and $\omega = 2\pi f$, but with a phase lag $\delta_\nu = \omega \Delta t$. The complex Poisson's ratio is the ratio of the lateral to the axial strains:

$$\bar{\nu}(j\omega) = \frac{\varepsilon_y(t)}{\varepsilon_x(t)} = \frac{\hat{\varepsilon}_y}{\hat{\varepsilon}_x} e^{-j\delta_\nu} = \frac{\hat{\varepsilon}_y}{\hat{\varepsilon}_x}(\cos\delta_\nu - j\sin\delta_\nu) = \nu_d(\omega) - j\nu_l(\omega) = \nu_d(\omega)[1 - j\eta_\nu(\omega)] \tag{4.2}$$

where ν_d is the dynamic Poisson s ratio, ν_l is the loss component, and η_ν is the Poisson's loss factor:

$$\eta_\nu(\omega) = \frac{\nu_l(\omega)}{\nu_d(\omega)} \tag{4.3}$$

The absolute value of $\bar{\nu}(j\omega)$ (Eqn. 4.2) provides an expression that relates ν_d and η_ν to the magnitude of the Poisson's ratio $|\bar{\nu}(j\omega)|$:

$$|\bar{\nu}(j\omega)| = \frac{\hat{\varepsilon}_y}{\hat{\varepsilon}_x} = (\nu_d^2 + \nu_l^2)^{1/2} = \nu_d(1 + \eta_\nu^2)^{1/2} \tag{4.4}$$

Further, it is shown in Ref. [Pritz, 2007] that, assuming an incompressible material ($\nu_d \approx 0.5$), the Poisson's lost factor relates to the materials' shear loss modulus η_G through the following expression:

$$\frac{\eta_\nu(\omega)}{\eta_G(\omega)} \approx 1 - 2\nu_d(\omega) \tag{4.5}$$

We obtained a set of experimental values for η_G by conducting a dynamic mechanical analysis (DMA) of the studied material. Fig. 4.13 presents the results. Measurements indicate an increase in the real part of the shear modulus G' and the shear loss modulus $\eta_G = G^{\text{“}}/G$ with increasing frequency. This phenomenon can be attributed to the polymer-particles and particle-particle interactions. [Frohlich et al., 2005]

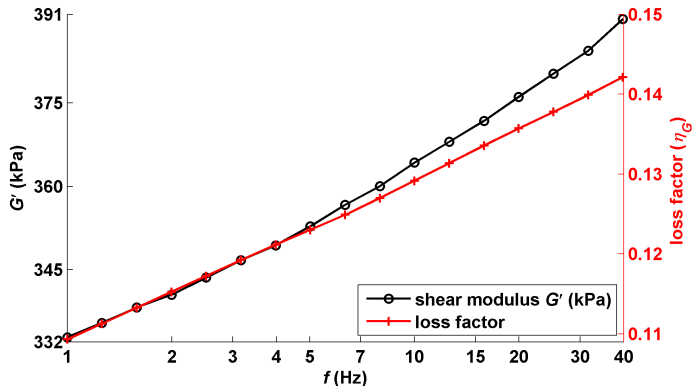

Figure 4.13: Storage moduli (G') and loss factor (η_G) as functions of frequency for the SEC composite (SEBS+TiO_2).

Values for η_G obtained from the DMA, combined with the experimental Poisson ratio coefficients derived from S and Eqn. 4.7, can be used with Eqns. 4.4 and 4.5 to find ν_d and η_ν. Figures. 4.14a and 4.14b show the results obtained over the frequency range 1-40

Hz. The red solid line is the data fit using a two-term power series fit. This fit can be used to characterize the changes in ν_d and η_ν as a function of ω, and yield mathematical expressions to generate the adjusted electromechanical model.

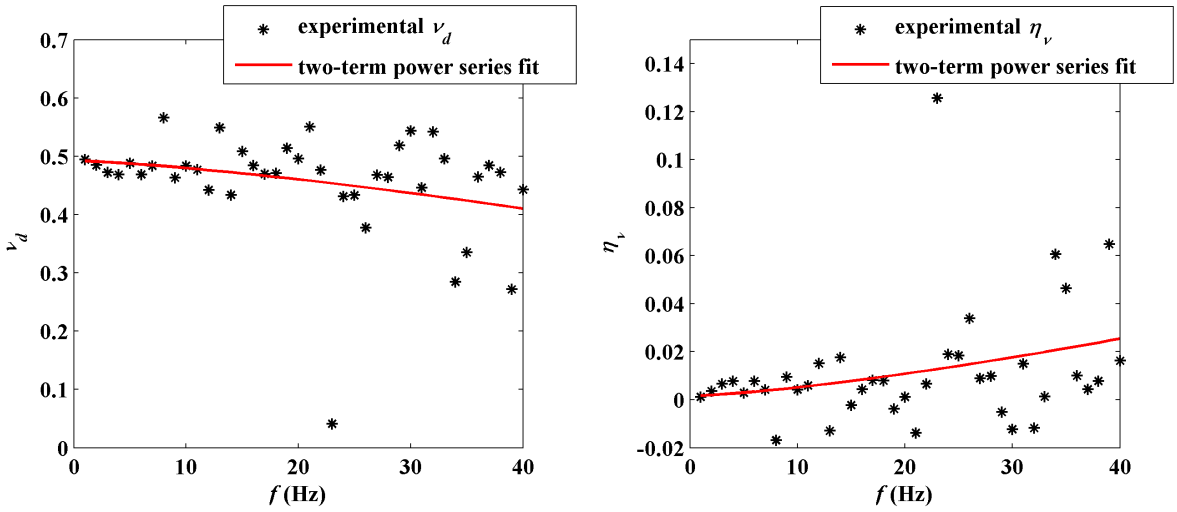

(a) (b)

Figure 4.14: a) Dynamic Poisson's ratio and b) Poisson's ratio loss factor plotted against frequency

4.3.3 Adjusted electromechanical model

Using results from the previous section, we can generate an adjusted electromechanical model that accounts for the change in the material's behavior as the frequency increases. The proposed model is a variation of Eqn. 4.6:

$$\frac{\Delta C}{C} = \lambda_{\text{adj}}(\varepsilon_x + \varepsilon_y) \tag{4.6}$$

where

$$\lambda_{\text{adj}} = \frac{1}{1 - \nu_{\text{adj}}} \tag{4.7}$$

and

$$\nu_{\text{adj}}(\omega) = \nu_d(\omega)(1 + \eta_\nu^2(\omega))^{1/2} \tag{4.8}$$

where the expressions for ν_d and η_ν are directly obtained from the investigation in the previous section:

$$\begin{aligned} \nu_d(\omega) &= -4.65 \times 10^{-5}\omega^{1.35} + 0.49 \\ \eta_\nu(\omega) &= 1.27 \times 10^{-5}\omega^{1.36} + 0.0016 \end{aligned} \tag{4.9}$$

where the adjusted electromechanical model is valid up to 40 Hz.

Figure 4.15 shows the RMSE on the estimation of λ as a function of frequency, for both the original and adjusted models. Table 4.1 summarizes the results for frequency ranges of interest. Results show that the adjusted model provides an overall improvement on the estimation of RMSE_λ by 14.3% over the range 1-40 Hz. The vast majority of this improvement is from the estimation in the 16-40 Hz range, where the adjusted model improves the estimation on RMSE_λ by 15.8%. This demonstrates the superiority of the new model over the original model. Note that the RMSE_λ over the range 1-15 Hz is only marginally improved, which demonstrates the validity of the original model over the 1-15 Hz range.

Table 4.1: Average RMSE_λ

	range		
	1-40 Hz	1-15 Hz	16-40 Hz
original model	0.266	0.146	0.317
adjusted model	0.228	0.143	0.267
improvement	14.3%	2.05%	15.8%

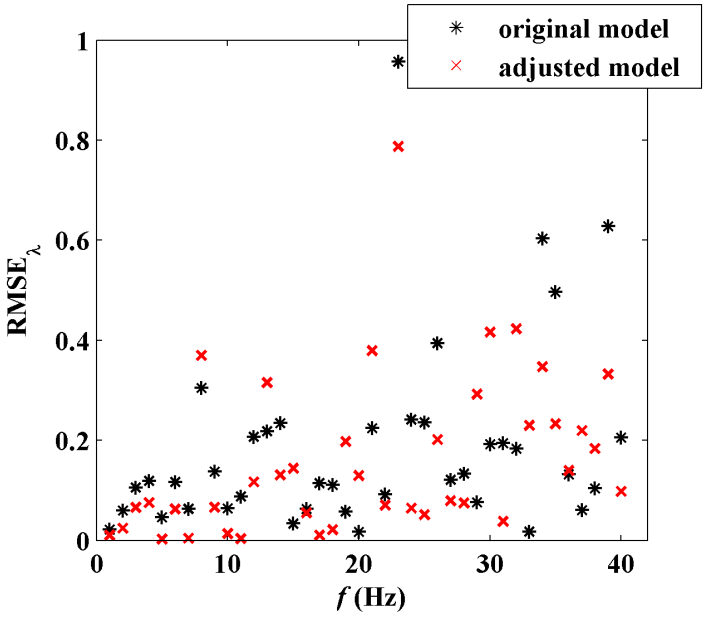

Figure 4.15: RMSE of the estimation of λ with varying frequency

4.3.4 Dynamic system identification

To examine the ability of the SEC to be used for Structural health monitoring applications, an experimental setup consisting of six SECs deployed on a 416 $\times$ 324 $\times$ 4 mm^3 cantilever fiberglass plate is built. The number of SECs was limited by the data acquisition system capacity used herein to read the SEC signals. To validate the SECs measurements, RSGs of 1 $\mu\varepsilon$ resolution were deployed around each SEC. An initial displacement of 3.8 cm was applied and the free vibration response of the plate was recorded at 250 Hz. Figure 4.16 shows the setup used to perform the free vibration experiment and a sketch of the SECs and the RSGs locations.

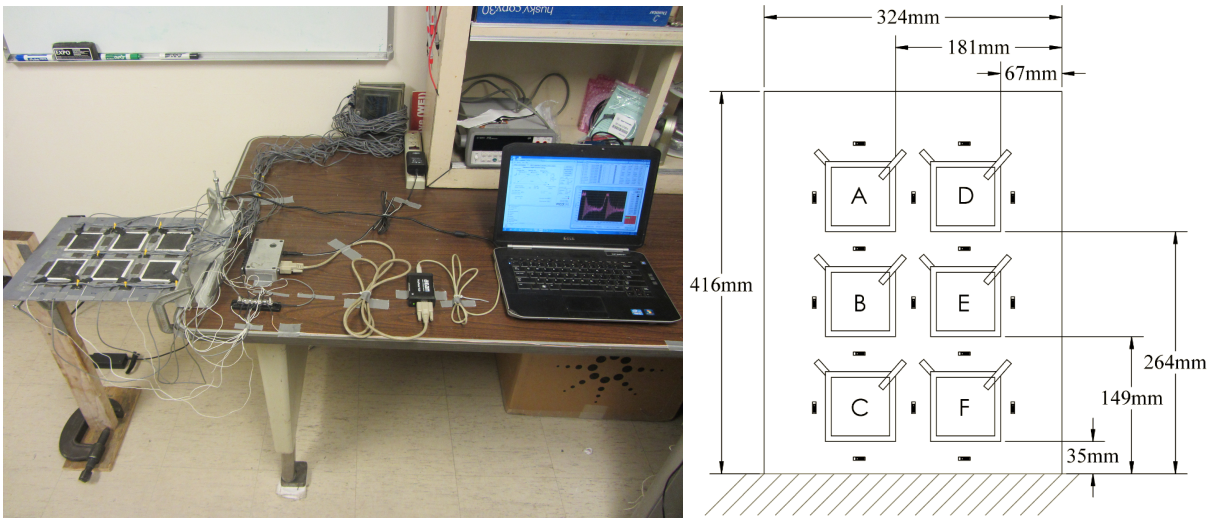

(a) (b)

Figure 4.16: Free vibration a) test setup and b) sketch

Figure 4.17 shows the time series of the SEC strain calculated using Eqn. (4.6) against the average additive measurements of the RSGs surrounding the edges of the SECs. The plots show three plateaus of strain reflecting the initial displaced state followed by a monotonically decreasing sinusoidal after the release of the plate edge. The variance of the SEC signal increases moving farther from the fixed end, toward the free end. This can be explained by the decrease in strain leading to a reduction in the signal to noise ratio (SNR). Results show good agreement between the strain readings as obtained from the electromechanical SEC model and the RSGs.

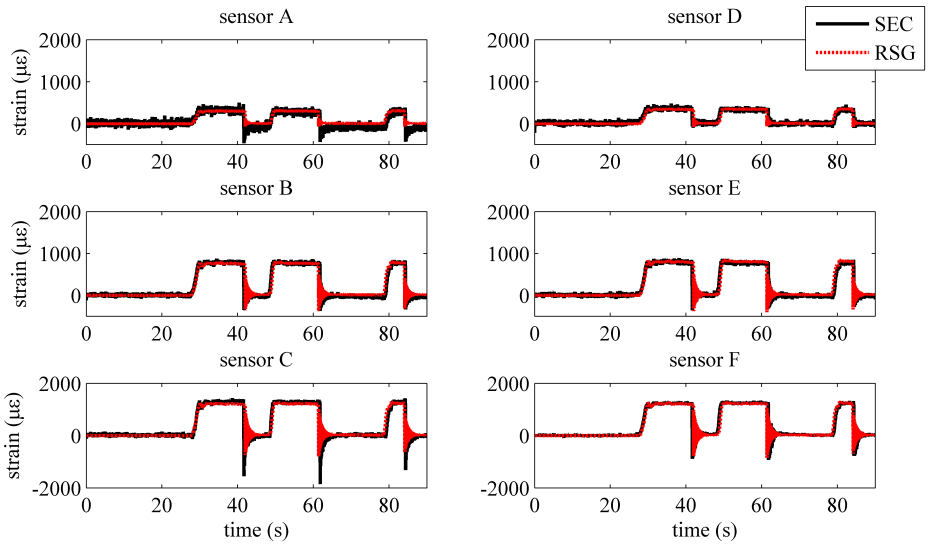

Figure 4.17: Free vibration test results

To assess the SECs capability in dynamic monitoring, the plate structure is modified by adding 1) a mass element and 2) a stiffness element. The objective was to change the dynamic properties of the plate and assess the capability of the SECs to track those changes. Table. 4.2 shows the location of the modifications made to the plate. The free vibration of the plate after release was studied for cases 1,2 and 3. Figure 4.18 shows the response of the SECs against the RSG for the initial state of the structure with no modifications. Similar to Figure 4.17 it can be noticed that the low SNR has resulted in a noisy signal for sensors A and D.

Table 4.2: Plate modifications

Case	Description
1	initial state
2	Mass at corner A
3	bar added to side A,B,C (mass+stiffness)

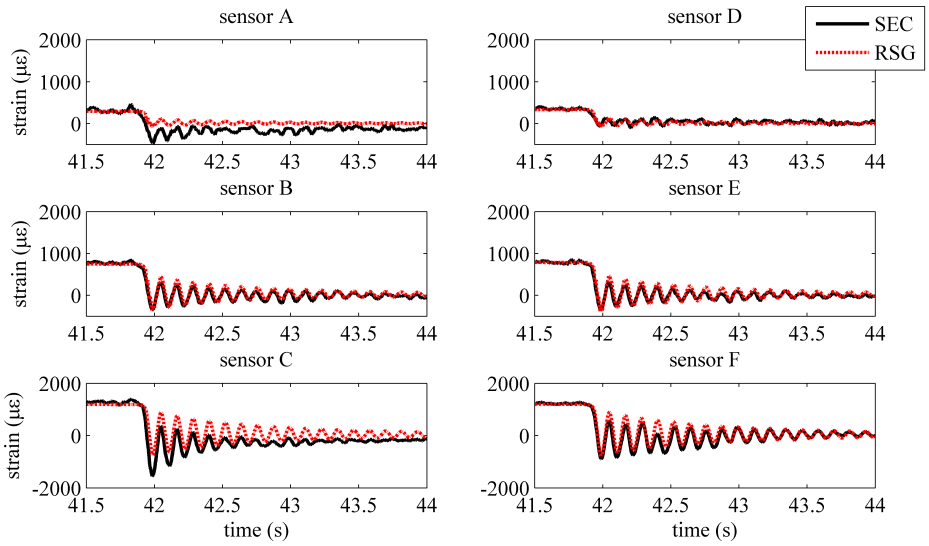

Figure 4.18: Free vibration results

The signal from each sensor and for each case is analyzed in the frequency domain. The frequency of the excitation and the corresponding energy content for each case and each sensor are extracted and compared. Figure 4.19a shows the Fourier Transform of the response signal obtained from the SECs for all the cases. The plots show the frequency of the first mode of vibration for the plate. The shift in the frequency is clearly noticed in the SECs except for sensors A and D where the noise content was large preventing accurate prediction of frequency content. To validate these predictions the response of the strain signal calculated using the RSGs is similarly analyzed and shown in Figure 4.19b. The results show very good agreement indicating the SECs ability to track frequency changes.

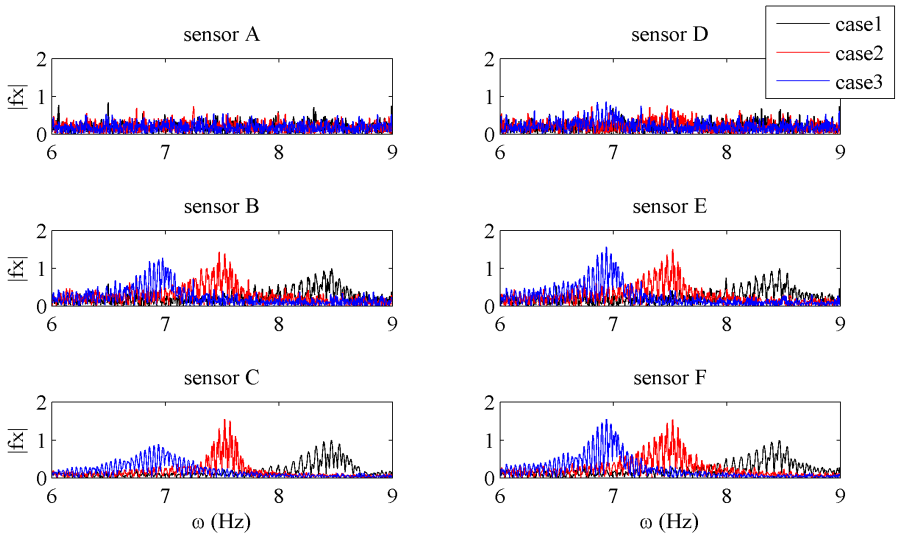

(a) Frequency change using SECs

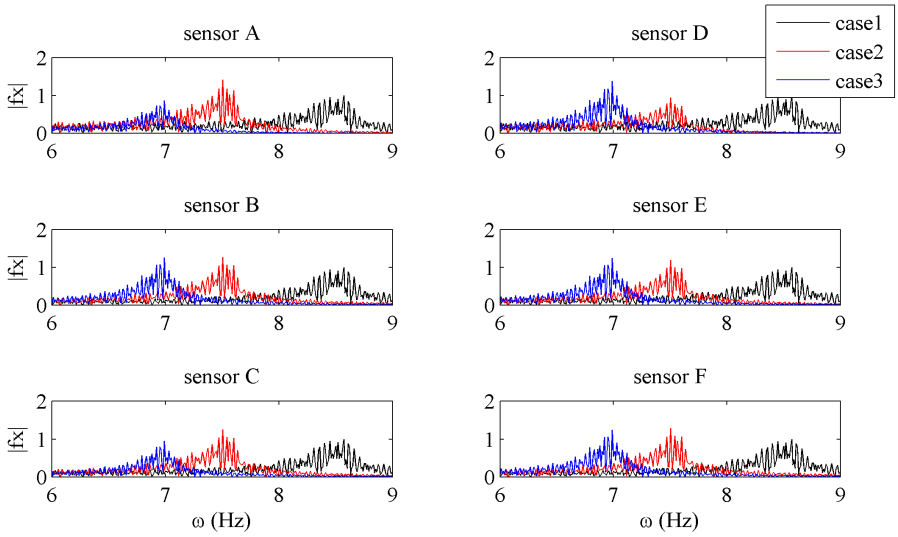

(b) Frequency change using RSGs

Figure 4.19: Frequency change using SECs and RSGs

4.4 Conclusion

- This chapter presented the characterization of a novel capacitive sensor designed to be used in a network setup.

- The electromechanical model for the SEC is experimentally validated with a quasi-static and a dynamic excitation.
- The model showed linear response using the quasi-static load and across the whole dynamic excitation spectrum of 1 to 40 Hz.
- The capability of the sensor to estimate the frequency content of the input excitation is also validated.
- A reduction in the sensitivity of the sensor is noticed, to explain this a reduction in the Poisson's ratio of the polymer composite is assumed as suggested in the literature.
- an adjusted electromechanical model that could account for linearities up to 40 Hz is presented. The modal was based on laboratory experiments.
- The SECs capability to track structural changes is investigated and a frequency change is detected due to an induced mass or stiffness change in the structure.
- The results we presented show promise for a wide range of structural health monitoring applications in large structures, such as civil infrastructure and wind turbine blades.
- Further investigation is needed in the area of the Poisson's ratio for the polymer.

CHAPTER 5. CONCLUSIONS AND FUTURE WORK

In this dissertation, a novel soft elastomeric capacitor sensor intended to be used in a network configuration to monitor large-scale systems is presented. The main advantages of such a sensor network is scalability, which leads to building a system capable of monitoring large structural systems with complex configurations efficiently. Other advantages include cost efficiency, customizability in size and shape, simple fabrication and installment and direct feature extraction with simple signal processing. The focus in this dissertation was on the development of the sensor, first to optimize its properties on the material level. Furthermore, the behavior of the sensor has been characterized to understand the output generated by the sensor and its relationship to the input. All this serves as a step forward into using the sensor in the field for SHM applications. To conclude this study, the major accomplishments/contributions are summarized in subsections 5.1-5.3 and future work is proposed in subsection 5.4.

5.1 Improved Fabrication process

To move from the relatively slow hazardous solution-cast method of fabrication, an improved high speed polymer processing techniques is proposed, termed as melt-mixing method,

- The process uses high-shear melt mixing technique followed by heat pressing the blend to thin films.

- The improvement in the dispersion increased the thermal stability and mechanical properties of the nanocomposite.
- These findings can lead to improved manufacturing processes for the soft capacitors, resulting in enhanced cost-effectiveness of the sensing method. Moreover, it facilitates transition into industry since its now possible to perform mass production.

5.2 Material Optimization

Two main properties are of interest to civil engineers when dealing with sensors; sensitivity and robustness. We investigated the effects of using different materials as additives to enhance the sensors properties. Specifically, the interfacial influence of TiO_2 and SEBS for melt-mixed nanocomposite dielectrics was of main focus. Here,

- Uncoated TiO_2 is compared with surface-treated TiO_2, and with a Si-69 enhanced SEBS solution.
- Morphology, mechanical, thermogravimetric, dynamic mechanical, and dielectric analyses are conducted on the prepared samples.
- Although using PDMS oil coated particles may not be the best in all the tests, the results show that these samples had overall superior performance, making this composition the optimum candidate to be used in the sensor fabrication.

5.3 Characterization of Behavior

The static and dynamic characterization of the sensor were performed. The main contributions can be summarized as follows:

- The theoretical electromechanical model for the SEC was experimentally validated with quasi-static and dynamic excitations.

- A linear response was observed using the quasi-static load and across the whole dynamic excitation spectrum of 1 to 40 Hz.
- The capability of the sensor to estimate the frequency content of the input excitation was established.
- A reduction in the sensitivity of the sensor was found, to explain this a reduction in the Poisson's ratio of the polymer composite is assumed as suggested in the literature.
- SECs capability to track structural changes was investigated and a frequency change was detected due to an induced mass or stiffness change in the structure.
- Results show promise for a wide range of structural health monitoring applications in large structures, such as civil infrastructure and wind turbine blades.

5.4 Future Work

The following items are recommended for future studies;

- Apply a SEC network on an actual full-scale blade to verify the capability of the network to build strain maps that can be used for extracting other features and for damage identification.
- Further investigate the Poisson's ratio variability for the polymer.
- Investigate insulation (shielding) of the SEC to reduce the noise, increase the accuracy and capability to measure smaller strains.
- Characterize the temperature effects, including electrical (i.e. change is sensitivity) and mechanical (i.e. effect of different coefficient of thermal expansion than steel/concrete), this is accomplished by measuring "apparent" thermal strains

caused by temperature changes when installed on various free (unrestrained) structural materials giving thermal correction factors

APPENDIX A. FABRICATION PROCESS

A.1 Introduction

This appendix further explains the solution cast fabrication process of the SEC in a more detailed manner. Materials and equipment required, and a step-by-step fabrication procedure are provided in this appendix.

A.2 Materials

This section describes the materials required in order to perform the complete fabrication process and production of SECs:

- **SEBS**:

  The thermoplastic matrix material SEBS-Mediprene 500120 M, (poly-Styrene-co-Ethylene-co-Butylene-co-Styrene) was purchased from VTC Elastoteknik AB, Sweden. (density = 930 kg/m). SEBS is used as the polymeric matrix. A picture of the purshased SEBS in shown in Figure. A.2a

- **Rutile titania (TiO_2)**:

  Rutile titania (TiO_2) namely R320, R320D (Sachtleben Chemie GmbH (Germany), are used as high permittivity fillers. The TiO_2 particles have an average diameter of 300 nm and density = 4200 kg/m3. While R320 is uncoated, R320D is coated with silicone oil (PDMS). Apicture of TiO_2 powder is shown in Figure. A.2b.

- **Chemicals**: Usually found in any general chemistry laboratory. Includes Toluene, Ethanol,Acetone, Methanol and Iso-Propyl as shown in Figure. A.1. Chemicals are required for several objectives including dissolving polymer and cleaning casting surfaces.

Figure A.1: Chemicals required for fabrication

- **Carbon Black**: Purchased from Orion Engineered Carbons, with spherical particles 24 μm in diameter and density of 1.89 g/cm^3. Figure. A picture is shown in A.2c.

(a) (b) (c)

Figure A.2: Pictures of (a) SEBS, (b) TiO_2 and (c) CB

- **Non-stick sheets**:

Non-porous PTFE coated fiberglass fabric (Teflon coating) are used as a non stick

surface covers. the sheets are obtained form Airtech industrial inc. CA, USA. the maximum temperature of use is 288 ^{o}C. Figure. A.3 shows a sample.

Figure A.3: Teflon sheet roll

- **Conductive tape**:

  Here copper tape is used. The tape is used to create the physical connection needed between the sensor it self and the data acquisition system (shown in Figure. A.4).

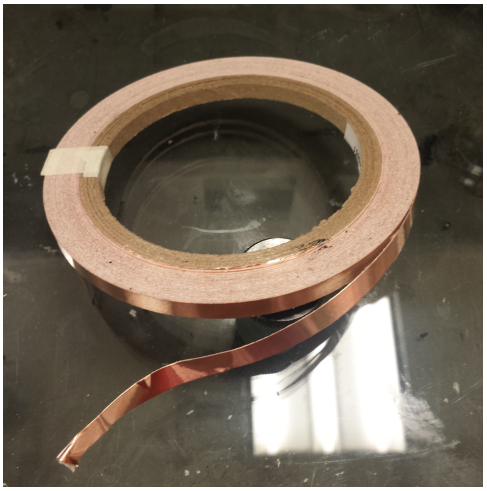

Figure A.4: Copper tape

A.3 equipment

- **Sonic Dismembrator and Sonic Bath**:

  The Sonic Dismembrator is bought from Fisher Scientific Model 120. While the Sonic bath is bought from Branson model 2800. Both uses the sonic ray technology to disperse particles inside a solution, the difference is that the dismembrator inputs larger amount of concentrated energy into the system in a short time while it takes a substantially longer time for the bath to deliver the same amount of energy. Both machines are shown in Figure. A.5

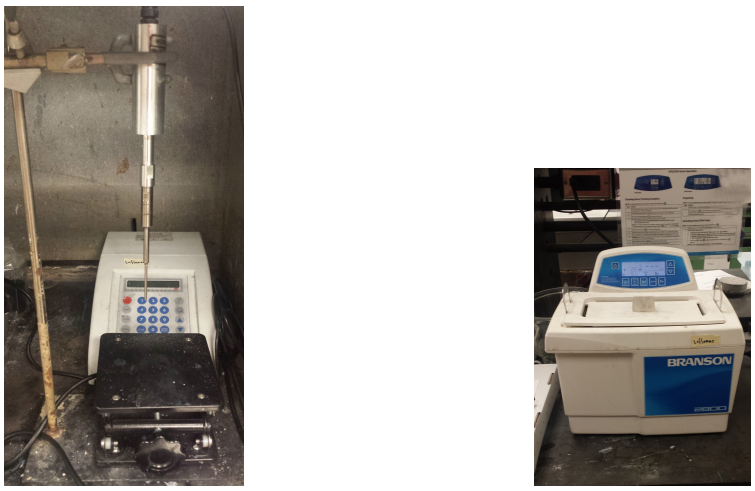

(a) (b)

Figure A.5: Pictures of a) sonic dismembrator and b) sonic bath

- **Leveled surface**:

  One of the most important items required for high accuracy is leveled surface for casting, here we manufacture a glass plate with three screws that changes the elevation of the plate from three corners until a leveled state is reached. the level is monitored by a circular level indicator. The system is shown in Figure. A.6.

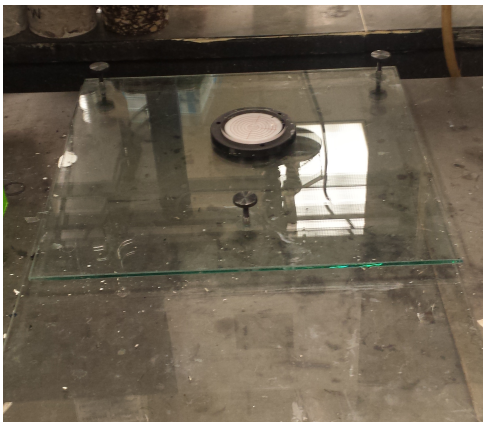

Figure A.6: Leveling system

- **Glass casting plates**:

  80×80 mm^2 (can be changed) flat glass plates are used for solution casting.

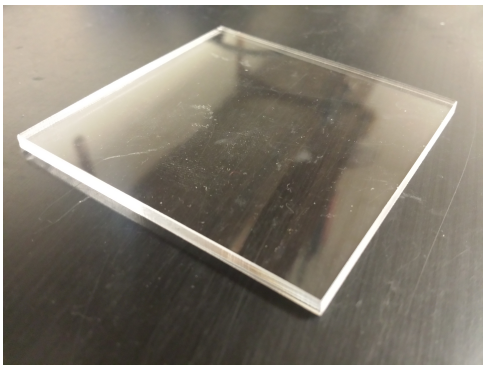

Figure A.7: Glass plate for casting

- **Fume hood**:

  Used for any operation dealing with small particles or solvents that may cause harm to users. It makes sure to keep any volatile substances or small particles contained inside the hood. (see Figure. A.8).

Figure A.8: A picture of a fume hood

- **General laboratory equipment**:

  Including, Flasks, para-film, vials, containers, balance, spatulas, pipettes, pipetter ,a multi-meter and a screw mircometer.

- **General safety equipment**:

  Including lab coat, gloves, safety goggles, and hear protection devices.

A.4 Procedure

The following is a step-by-step procedure on how to make a single SEC.

Note 1: whenever weighing is required, it is always necessary to tare the balance with the container on the balance before adding any material.

Note 2: This is a 2 day minimum process.

A.4.1 Step 0: Preparing casting surfaces

Before starting to create any solutions or mixes, Casting plates are prepared. The glass plates available in glass shops causes the processed material to stick to the surface, making it vulnerable to be torn or damaged. To over come this issue we cover the surface with a Teflon sheet as follows.

- Using a razor, cut a Teflon sheet to exactly match the surface area of the glass plate.
- Use elmers glue (or a similar product) to cover the glass surface with a light layer. Adhere the Teflon sheet to the glass surface and remove any air voids between the sheet and the glass surface using a squeegee. Wait for a few minutes.
- Clean the surface of the Teflon sheet adhered on the glass plate with acetone, ethanol and propanol. This will eliminate any organic substance on the surface.

  After cleaning, the plate(s) is placed on the leveled glass surface. Leveling the surface is an extremely essential part of the whole process, it makes sure the liquid casted on the glass plate is leveled, therefore it will have a constant thickness when it dries and becomes a film.

A.4.2 Step 1: Create solutions

The first step is to dissolve the SEBS by an organic solvent (Toluene) and create the SEBS solution. Two solutions are prepared in this step, one for creating the dielectric and the other is for creating the conductive solution. we use SEBS120 for the dielectric solution and SEBS50 for the conductive solution.

The portions of each material to add (SEBS and Toluene) will depend on the desired flowability of the solution to be made, which will reflect on the volume of the solution required to make a specific volume of solid material. The following portions are made

after a few trials and a desired flowability is reached. The conductive solution is made thicker since ultimately it will be brushed on the dielectric, therefore it is desirable for it to be viscous.

- Dielectric solution:
  - Add 250 *ml* of Toluene measured in a graduated flask to 30.5 g of SEBS120.
  - Use para film to seal the container and leave it over night to dissolve.
- Conductive solution:
  - Add 100 *ml* of Toluene measured in a graduated flask to 30 g of SEBS50.
  - Use para film to seal the container and leave it over night to dissolve.

A.4.3 Step 2: Create mixes

The second step is to dope the solutions. One with high permitivitty particles to create the dielectric mix, here we are using TiO_2. And the second with highly conductive material to create a conductive mix, here we are using carbon black (CB).

- Dielectric mix:
  - Add 15 *ml* of the dielectric solution using a pipette to 1.29 g of TiO_2 weighed in a vial.
  - Use para film to seal the vial until needed for use.
- Conductive mix:
  - Add 15 *ml* of conductive solution using a pipette to 0.7 g of CB weighed in a vial.
  - Use para film to seal the container.

Figure. A.9 shows the both mixes.

(a) (b)

Figure A.9: Pictures of a) TiO_2 mix and b) CB mix

A.4.4 Step 3: Dispersion

The third step is to disperse the particles we have doped in the polymeric matrix. To do this, we will perform the following steps:

- Dielectric mix:
  - Get a container with a size larger than the vial. Fill it with crushed ice and add some water. This ice bath is to be used when ever using the sonic dismembrator. This is to prevent any over heating in the samples, thus avoiding polymer degradation.
  - Place the vial inside the ice bath and sonicate the mix inside the vial with the tip of the sonic dismembrator for 10 min.
- Conductive mix: **Note:** This step is done on the day the conductive mix is required.
  - Place the sealed vial in the sonic bath for 5 hours followed by 5 minutes using the sonic tip (while the vial is in the ice bath).
  - Use a brush to take a sample and put it on a weighting paper. Wait for a few minutes for it to dry and measure the resistivity. If it is less than 5 $k\Omega$/square,

the mix is well dispersed. If not, place the vial in the sonic dismembrator for 5 more minutes.

A.4.5 Step 4: Casting the dielectric

The fourth step is to cast the dielectric solution we prepared in Step 3. The following steps describe how.

- Using a pipette draw 10 *ml* of the dispersed dielectric mix.
- Start casting the liquid on the covered glass plates starting with the edges going inwards (see Figure. A.10.
- After casting all the pipete's contents. Use two other glass plates to tap on the sides of the plate you just used for casting. This will create some vibration to help distribute the mix as even as possible.
- Cover the casted plate with a paper box to slow down the evaporation rate of the toluene. The sample will be dry the next day.

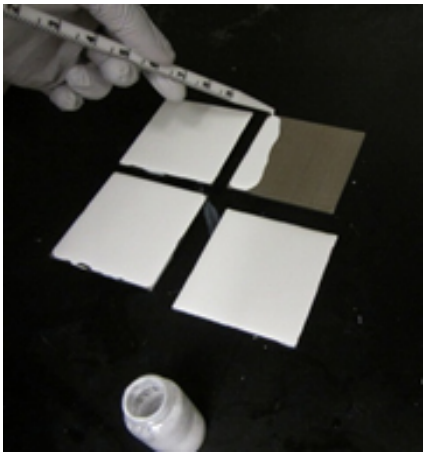

Figure A.10: Casting process

A.4.6 Step 5: Quality test

The fifth step is to test the uniformity of the thickness of the dried film. This is done as follows

- Remove the film from the glass plate and place it between two teflon sheet with a size slightly larger than the film.
- Use a screw mircometer to measure the thickness of two standalone teflon sheets, then zero the gauge.
- Use the zerod micrometer to measure the thickness of the film covered with two teflon sheets. take at least 9 measurements in 9 different locations within the surface area.
- Calculate the difference between the minimum and the maximum value, if it is less then 10 % of the average accept the film, otherwise reject.

A.4.7 Step 6: Preparation for electrode application

The sixth step is to prepare the films for the electrode layer application. This is done as follows

- Cut a teflon sheet with a size similar to the film.
- Using the same sheet, make an inside cut with the size 65 $\times$ 65 mm^2. keep the outer part, let call it a mold.
- Uncover one side of the film and place the mold on top of the film so that the covered edges are equal is width(s).
- Use scotch tape and tape all the edges tightly.

A.4.8 Step 7: Casting the dielectric

The seventh step is to paint the films with the electrodes, top and bottom using a brush and connect the copper tape. This is done as follows

- Before starting make sure the brush in use is clean. if not immerse it in some toluene to clean it.
- Start by painting a very this layer by carrying just a small amount of liquid in the brush.
- wait for a few minutes and brush the surface again. Wait again.
- After the second layer of paint, get a 4 cm long copper tape and place it on the right corner of the sensor diagonally as shown in Figure. 1.1a.
- Following the same fashion, apply two more layers. Wait for at least one hour.
- Repeat steps 6 and 7 for the other side.

A.4.9 Step 8: Testing of the sensor

The final step is to check if the sensor actually works, this is done by measuring the capacitance using the copper tapes attached earlier. If the capacitance value is positive, Accept. Otherwise reject.

The final product is shown in Figure. 1.1a.

REFERENCES

[Frohlich et al., 2005] J. Fröhlich, W. Niedermeier, H.-D. Luginsland, The effect of filler–filler and filler–elastomer interaction on rubber reinforcement, Composites Part A: Applied Science and Manufacturing 36 (4) (2005) 449–460.

[Arms et al., 2009] Arms, S., Galbreath, J., Townsend, C., Churchill, D., Corneau, B., Ketcham, R., and Phan, N. (2009). Energy harvesting wireless sensors and networked timing synchronization for aircraft structural health monitoring. In *Wireless Communication, Vehicular Technology, Information Theory and Aerospace & Electronic Systems Technology, 2009. Wireless VITAE 2009. 1st International Conference on*, pages 16–20. IEEE.

[Arshak et al., 2000] Arshak, K., McDonagh, D., and Durcan, M. (2000). Development of new capacitive strain sensors based on thick film polymer and cermet technologies. *Sensors and Actuators A: Physical*, 79(2):102 – 114.

[B. Srensen and Rusborg, 2002] B. Srensen, L.L., P. S. M. M. C. D. O. K. G. L. A. H. J. R. and Rusborg, J. (2002). Fundamentals for remote structural health moni-toring of wind turbine blades-a preproject. *Ris National Laboratory*.

[Balageas et al., 2006] Balageas, D., Fritzen, C.-P., and Güemes, A. (2006). *Structural health monitoring*, volume 493. Wiley Online Library.

[Baptista et al., 2009] Baptista, F. G. et al. (2009). A new impedance measurement system for pzt-based structural health monitoring. *Instrumentation and Measurement, IEEE Transactions on*, 58(10):3602–3608.

[Bockstaller et al., 2005] Bockstaller, M. R., Mickiewicz, R. A., and Thomas, E. L. (2005). Block copolymer nanocomposites: perspectives for tailored functional materials. *Advanced Materials*, 17(11):1331–1349.

[Bruggeman, 1935] Bruggeman, D. A. G. (1935). Berechnung verschiedener physikalischer konstanten von heterogenen substanzen. i. dielektrizittskonstanten und leitfhigkeiten der mischkrper aus isotropen substanzen. *Annalen der Physik*, 416(7):636–664.

[Cava et al., 1995] Cava, R., Peck, W., and Krajewski, J. (1995). Enhancement of the dielectric constant of ta2o5through substitution with tio2.

[Chang et al., 2003] Chang, P. C., Flatau, A., and Liu, S. C. (2003). Review paper: Health monitoring of civil infrastructure. *Structural Health Monitoring*, 2(3):257–267.

[Choi et al., 2008] Choi, H., Choi, S., and Cha, H. (2008). Structural health monitoring system based on strain gauge enabled wireless sensor nodes. In *Networked Sensing Systems, 2008. INSS 2008. 5th International Conference on*, pages 211–214. IEEE.

[C.R. Farrar and Robertson, 2003] C.R. Farrar, H. Sohn, F. H. M. A. M. B. P. C. S. D. J. S. N. L. and Robertson, A. (2003). Damage prognosis: current status and future needs. Technical Report LA-14051-MS, Los Alamos National Laboratory.

[Dang et al., 2008] Dang, Z.-M., Yu, Y.-F., Xu, H.-P., and Bai, J. (2008). Study on microstructure and dielectric property of the batio 3/epoxy resin composites. *Composites Science and Technology*, 68(1):171–177.

[Dobrzynska and Gijs, 2013] Dobrzynska, J. A. and Gijs, M. A. M. (2013). Polymer-based flexible capacitive sensor for three-axial force measurements. *Journal of Micromechanics and Microengineering*, 23(1):015009.

[Farrar and Worden, 2007] Farrar, C. R. and Worden, K. (2007). An introduction to structural health monitoring. *Philosophical Transactions of the Royal Society of London A: Mathematical, Physical and Engineering Sciences*, 365(1851):303–315.

[Ganguly et al., 2006] Ganguly, A., De Sarkar, M., and Bhowmick, A. K. (2006). Thermoplastic elastomeric nanocomposites from poly [styrene–(ethylene-co-butylene)–styrene] triblock copolymer and clay: Preparation and characterization. *Journal of applied polymer science*, 100(3):2040–2052.

[Gao et al., 2010] Gao, L., Thostenson, E. T., Zhang, Z., Byun, J.-H., and Chou, T.-W. (2010). Damage monitoring in fiber-reinforced composites under fatigue loading using carbon nanotube networks. *Philosophical Magazine*, 90(31-32):4085–4099.

[Hadži, 1961] Hadži, D. (1961). Far-infrared bands of some crystals with strong hydrogen bonds. *The Journal of Chemical Physics*, 34(4):1445–1445.

[Hashimoto et al., 1981] Hashimoto, H., Fujimura, M., Hashimoto, T., and Kawai, H. (1981). Domain-boundary structure of styrene-isoprene block copolymer films cast from solutions. 7. quantitative studies of solubilization of homopolymers in spherical domain system. *Macromolecules*, 14(3):844–851.

[Ho et al., 2013] Ho, X., Tey, J. N., Liu, W., Cheng, C. K., and Wei, J. (2013). Biaxially stretchable silver nanowire transparent conductors. *Journal of Applied Physics*, 113(4):044311.

[Hong et al., 2012] Hong, H. P., Jung, K. H., Min, N. K., Rhee, Y. H., and Park, C. W. (2012). A highly fast capacitive-type humidity sensor using percolating carbon nanotube films as a porous electrode material. In *Sensors, 2012 IEEE*, pages 1–4.

[Huang et al., 2003] Huang, C., Zhang, Q., and Su, J. (2003). High-dielectric-constant all-polymer percolative composites. *Applied Physics Letters*, 82(20):3502–3504.

[Ismail et al., 2002] Ismail, H., Shuhelmy, S., and Edyham, M. (2002). The effects of a silane coupling agent on curing characteristics and mechanical properties of bamboo fibre filled natural rubber composites. *European Polymer Journal*, 38(1):39–47.

[Jones, 2009] Jones, G. (2009). Small turbine blade inspection using laser strain techniques. 51(3):137.

[Kang et al., 2006] Kang, I., Schulz, M. J., Kim, J. H., Shanov, V., and Shi, D. (2006). A carbon nanotube strain sensor for structural health monitoring. *Smart Materials and Structures*, 15(3):737.

[Kollosche et al., 2011] Kollosche, M., Stoyanov, H., Laflamme, S., and Kofod, G. (2011). Strongly enhanced sensitivity in elastic capacitive strain sensors. *J. Mater. Chem.*, 21(23):8292–8294.

[Krishnamoorti et al., 2001] Krishnamoorti, R., Silva, A. S., and Mitchell, C. A. (2001). Effect of silicate layer anisotropy on cylindrical and spherical microdomain ordering in block copolymer nanocomposites. *The Journal of Chemical Physics*, 115(15):7175–7181.

[Kugler et al., 1990] Kugler, H. P., Stacer, R. G., and Steimle, C. (1990). Direct measurement of poisson's ratio in elastomers. *Rubber Chemistry and Technology*, 63(4):473–487.

[Lading et al., 2002] Lading, L., McGugan, M., Sendrup, P., Rheinlnder, J., and Rusborg, J. (2002). *Fundamentals for remote structural health monitoring of wind turbine blades - a preproject. Annex B. Sensors and non-destructive testing methods for damage detection in wind turbine blades.* Denmark. Forskningscenter Risoe. Risoe-R.

[Laflamme et al., 2012] Laflamme, S., Kollosche, M., Connor, J. J., and Kofod, G. (2012). Robust flexible capacitive surface sensor for structural health monitoring applications. *Journal of Engineering Mechanics*, 139(7):879–885.

[Laflamme et al., 2013a] Laflamme, S., Saleem, H., Vasan, B., Geiger, R., Chen, D., Kessler, M., and Rajan, K. (2013a). Soft elastomeric capacitor network for strain sensing over large surfaces. *Mechatronics, IEEE/ASME Transactions on*, 18(6):1647–1654.

[Laflamme et al., 2013b] Laflamme, S., Saleem, H. S., Vasan, B. K., Geiger, R. L., Chen, D., Kessler, M. R., and Rajan, K. (2013b). Soft elastomeric capacitor network for strain sensing over large surfaces. *Mechatronics, IEEE/ASME Transactions on*, 18(6):1647–1654.

[Laflamme et al., 2014] Laflamme, S., Ubertini, F., Saleem, H., DAlessandro, A., Downey, A., Ceylan, H., and Materazzi, A. L. (2014). Dynamic characterization of a soft elastomeric capacitor for structural health monitoring. *Journal of Structural Engineering*.

[Laurer et al., 1996] Laurer, J. H., Bukovnik, R., and Spontak, R. J. (1996). Morphological characteristics of sebs thermoplastic elastomer gels. *Macromolecules*, 29(17):5760–5762.

[Lee et al., 2003] Lee, J. Y., Park, M. S., Yang, H. C., Cho, K., and Kim, J. K. (2003). Alignment and orientational proliferation of hex cylinders in a polystyrene-block-polyisoprene-block-polystyrene copolymer in the presence of clay. *Polymer*, 44(5):1705–1710.

[Lipert et al., 2002] Lipert, R. J., Shinar, R., Vaidya, B., Pris, A. D., Porter, M. D., Liu, G., Grabau, T. D., and Dilger, J. P. (2002). Thin films of block copolymer blends for

enhanced performance of acoustic wave-based chemical sensors. *Analytical chemistry*, 74(24):6383–6391.

[Lipomi et al., 2011] Lipomi, D. J., Vosgueritchian, M., Tee, B. C. K., Hellstrom, S. L., Lee, J. A., Fox, C. H., and Bao, Z. (2011). Skin-like pressure and strain sensors based on transparent elastic films of carbon nanotubes. *Nature Nanotechnology*, 6(12):788–792.

[Maenaka, 2008] Maenaka, K. (2008). Mems inertial sensors and their applications. In *Networked Sensing Systems, 2008. INSS 2008. 5th International Conference on*, pages 71–73. IEEE.

[Mani et al., 2000] Mani, S., Weiss, R., Cantino, M., Khairallah, L., Hahn, S., and Williams, C. (2000). Evidence for a thermally reversible order–order transition between lamellar and perforated lamellar microphases in a triblock copolymer. *European polymer journal*, 36(1):215–219.

[Mc Carthy et al., 2009] Mc Carthy, D., Risse, S., Katekomol, P., and Kofod, G. (2009). The effect of dispersion on the increased relative permittivity of tio2/sebs composites. *Journal of Physics D: Applied Physics*, 42(14):145406.

[Michie et al., 1997] Michie, W., Thursby, G., Walsh, D., Culshaw, B., and Konstantaki, M. (1997). Distributed sensing of physical and chemical parameters for structural monitoring.

[Mischenko et al., 1994] Mischenko, N., Reynders, K., Mortensen, K., Scherrenberg, R., Fontaine, F., Graulus, R., and Reynaers, H. (1994). Structural studies of thermoplastic triblock copolymer gels. *Macromolecules*, 27(8):2345–2347.

[Nelson and Kutty, 2004] Nelson, P. and Kutty, S. (2004). Cure characteristics and mechanical properties of maleic anhydride grafted reclaimed rubber/styrene butadiene rubber blends. *Polymer-Plastics Technology and Engineering*, 43(1):245–260.

[Panda et al., 2008] Panda, M., Srinivas, V., and Thakur, A. (2008). On the question of percolation threshold in polyvinylidene fluoride/nanocrystalline nickel composites. *Applied Physics Letters*, 92(13):132905–132905.

[Pritz, 2007] Pritz, T. (2007). The poisson's loss factor of solid viscoelastic materials. *Journal of Sound and Vibration*, 306(35):790 – 802.

[Ren et al., 2000] Ren, J., Silva, A. S., and Krishnamoorti, R. (2000). Linear viscoelasticity of disordered polystyrene-polyisoprene block copolymer based layered-silicate nanocomposites. *Macromolecules*, 33(10):3739–3746.

[Rytter, 1993] Rytter, A. (1993). *Vibrational Based Inspection of Civil Engineering Structures*. PhD thesis. Ph.D.-Thesis defended publicly at the University of Aalborg, April 20, 1993 PDF for print: 206 pp.

[Saleem et al., 2013] Saleem, H., Thunga, M., Kollosche, M., Kessler, M., and Laflamme, S. (2013). Bio-inspired sensory membrane: Fabrication processes for full-scale implementation. In *American Institute of Physics Conference Series*, volume 1511, pages 1601–1608.

[Schubel et al., 2013] Schubel, P., Crossley, R., Boateng, E., and Hutchinson, J. (2013). Review of structural health and cure monitoring techniques for large wind turbine blades. *Renewable Energy*, 51(0):113 – 123.

[Shankar et al., 2008] Shankar, R., Krishnan, A. K., Ghosh, T. K., and Spontak, R. J. (2008). Triblock copolymer organogels as high-performance dielectric elastomers. *Macromolecules*, 41(16):6100–6109.

[Silva et al., 2001] Silva, A. S., Mitchell, C. A., Tse, M. F., Wang, H.-C., and Krishnamoorti, R. (2001). Templating of cylindrical and spherical block copolymer microdomains by layered silicates. *The Journal of Chemical Physics*, 115(15):7166–7174.

[Smith et al., 2008] Smith, R., Liang, C., Landry, M., Nelson, J., and Schadler, L. (2008). The mechanisms leading to the useful electrical properties of polymer nanodielectrics. *Dielectrics and Electrical Insulation, IEEE Transactions on*, 15(1):187–196.

[Srivastava et al., 2011] Srivastava, R. K., Vemuru, V. S. M., Zeng, Y., Vajtai, R., Nagarajaiah, S., Ajayan, P. M., and Srivastava, A. (2011). The strain sensing and thermalmechanical behavior of flexible multi-walled carbon nanotube/polystyrene composite films. *Carbon*, 49(12):3928 – 3936.

[Stoyanov et al., 2011] Stoyanov, H., Kollosche, M., Risse, S., McCarthy, D. N., and Kofod, G. (2011). Elastic block copolymer nanocomposites with controlled interfacial interactions for artificial muscles with direct voltage control. *Soft Matter*, 7(1):194–202.

[Suster et al., 2006] Suster, M., Guo, J., Chaimanonart, N., Ko, W., and Young, D. (2006). A high-performance mems capacitive strain sensing system. *Microelectromechanical Systems, Journal of*, 15(5):1069–1077.

[Thomson et al., 2009] Thomson, D., Card, D., and Bridges, G. (2009). Rf cavity passive wireless sensors with time-domain gating-based interrogation for shm of civil structures. *Sensors Journal, IEEE*, 9(11):1430–1438.

[Tschoegl et al., 2002] Tschoegl, N., Knauss, W., and Emri, I. (2002). Poisson's ratio in linear viscoelasticity a critical review. *Mechanics of Time-Dependent Materials*, 6(1):3–51.

[Ubertini et al., 2014] Ubertini, F., Laflamme, S., Ceylan, H., Materazzi, A. L., Cerni, G., Saleem, H., DAlessandro, A., and Corradini, A. (2014). Novel nanocomposite technologies for dynamic monitoring of structures: a comparison between cement-based embeddable and soft elastomeric surface sensors. *Smart Materials and Structures*, 23(4):045023.

[Van Dijk and Van den Berg, 1995] Van Dijk, M. and Van den Berg, R. (1995). Ordering phenomena in thin block copolymer films studied using atomic force microscopy. *Macromolecules*, 28(20):6773–6778.

[Wada et al., 1962] Wada, Y., Ito, R., and Ochiai, H. (1962). Comparison between mechanical relaxations associated with volume and shear deformations in styrene-butadiene rubber. *Journal of the Physical Society of Japan*, 17(1):213–218.

[Wang and Dang, 2005] Wang, L. and Dang, Z.-M. (2005). Carbon nanotube composites with high dielectric constant at low percolation threshold. *Applied physics letters*, 87(4):042903.

[Wilkinson et al., 2004] Wilkinson, A., Clemens, M., and Harding, V. (2004). The effects of sebs-g-maleic anhydride reaction on the morphology and properties of polypropylene/pa6/sebs ternary blends. *Polymer*, 45(15):5239 – 5249.

[Worden and Dulieu-Barton, 2004] Worden, K. and Dulieu-Barton, J. M. (2004). An overview of intelligent fault detection in systems and structures. *Structural Health Monitoring*, 3(1):85–98.

[Yan et al., 2014] Yan, C., Wang, J., Kang, W., Cui, M., Wang, X., Foo, C. Y., Chee, K. J., and Lee, P. S. (2014). Highly stretchable piezoresistive graphene–nanocellulose nanopaper for strain sensors. *Advanced Materials*, 26(13):2022–2027.

[Yao and Zhu, 2014] Yao, S. and Zhu, Y. (2014). Wearable multifunctional sensors using printed stretchable conductors made of silver nanowires. *Nanoscale*, 6(4):2345–2352.

[Yoda, 1998] Yoda, R. (1998). Elastomers for biomedical applications. *Journal of Biomaterials Science, Polymer Edition*, 9(6):561–626.

[Zeman, 2007] Zeman, S. (2007). High energy density materials (structure and bonding). *Springer-Verlag: Heidelberg, Germany*, 125:195–271.

[Zhang et al., 2010] Zhang, Y., Tsai, J., Li, G.-P., Feng, M. Q., and Bachman, M. (2010). Moems acoustic sensors for structural health monitoring. In *Sensors, 2010 IEEE*, pages 2311–2315. IEEE.